1 # Highly time-resolved urban aerosol characteristics during

2 ## springtime in Yangtze River Delta, China: Insights from soot

3 ## particle aerosol mass spectrometry

5 Junfeng Wang,[1] Xinlei Ge,[1,]* Yanfang Chen,[1] Yafei Shen,[1] Qi Zhang,[1,2] Yele Sun,[3]

6 Jianzhong Xu,[4] Shun, Ge,[5] Huan Yu,[1] Mindong Chen[1,*]

8 [1]Jiangsu Key Laboratory of Atmospheric Environment Monitoring and Pollution

9 Control (AEMPC), Collaborative Innovation Center of Atmospheric Environment and

10 Equipment Technology (CIC-AEET), School of Environmental Science and

11 Engineering, Nanjing University of Information Science & Technology, Nanjing

12 210044, China

13 [2]Department of Environmental Toxicology, University of California at Davis, Davis,

14 California 95616, United States

15 [3]State Key Laboratory of Atmospheric Boundary Layer Physics and Atmospheric

16 Chemistry, Institute of Atmospheric Physics, Chinese Academy of Sciences, Beijing

17 100029, China

18 [4]State Key Laboratory of Cryospheric Sciences, Cold and Arid Regions,

19 Environmental and Engineering Research Institute, Chinese Academy of Sciences,

20 Lanzhou 730000, China

21 [5]Nanjing Tianbo Environmental Technology Co., Ltd, Nanjing 210047, China

23 *Corresponding author, Email: caxinra@163.com; chenmdnuist@163.com

24 Phone: +86-25-58731394

26 For *Atmos. Chem. Phys.*

Abstract: In this work, the Aerodyne soot particle – aerosol mass spectrometer (SP-AMS) was deployed for the first time during the spring of 2015 in urban Nanjing, a megacity in the Yangtze River Delta (YRD) of China, for online characterization of the submicron aerosols (PM_1). The SP-AMS enables real-time and fast quantification of refractory black carbon (rBC) simultaneously with other non-refractory species (ammonium, sulfate, nitrate, chloride and organics). The average PM_1 concentration was found to be 28.2 μg m^{-3}, with organics (45%) as the most abundant component, following by sulfate (19.3%), nitrate (13.6%), ammonium (11.1%), rBC (9.7%) and chloride (1.3%). These PM_1 species together can reconstruct ~44% of the light extinction during this campaign based on the IMPROVE method. Chemically-resolved mass-based size distributions revealed that small particles especially ultrafine ones (<100 nm vacuum aerodynamic diameter) were dominated by organics and rBC, while large particles had significant contributions from secondary inorganic species. Source apportionment of organic aerosols (OA) yielded four OA subcomponents, including hydrocarbon-like OA (HOA), cooking-related OA (COA), semi-volatile oxygenated OA (SV-OOA), and low-volatility oxygenated OA (LV-OOA). Overall, secondary organic aerosol (SOA, equal to the sum of SV-OOA and LV-OOA) dominated the total OA mass (55.5%), but primary organic aerosol (POA, equal to the sum of HOA and COA) can outweigh SOA in early morning and evening due to enhanced human activities. High OA concentrations were often associated with high mass fractions of POA and rBC, indicating the important role of anthropogenic emissions during heavy pollution events. The diurnal cycles of nitrate, chloride and SV-OOA both showed good anti-correlations with air temperatures, suggesting their variations were likely driven by thermodynamic equilibria and gas-to-particle partitioning. On the other hand, in contrast to other species, sulfate and LV-OOA concentrations increased during afternoon, and showed no positive correlations with relative humidity (RH), likely indicating the contribution from photochemical oxidation is dominant over that of aqueous-phase processing for their formations. The bivariate polar plots show that the SV-OOA was formed locally, and

the variations of hydrogen-to-carbon (H/C) and oxygen-to-carbon (O/C) ratios in the

Van Krevelen space further suggests an evolution pathway of SV-OOA to LV-OOA.

Our findings regarding springtime aerosol chemistry in Nanjing may have important

implications for the air quality remediation in the densely populated regions.

1. Introduction

In recent years, high concentrations of fine particulate matter ($PM_{2.5}$) have been

frequently observed (Hu et al., 2015), in accompanying with the visibility impairment

and occurrence of haze events across large parts of China. $PM_{2.5}$ also affects human

health (e.g., Pope and Dockery, 2006;Cao et al., 2012), regional and global climate

directly by absorbing and scattering solar radiation or indirectly by acting as cloud

condensation nuclei and ice nuclei (e.g.,Ghan and Schwartz, 2007;Pöschl, 2005), and

the earth's ecosystem (Carslaw et al., 2010). These effects are predominantly

dependent upon the physical and chemical characteristics of fine particles, such as

mass concentration, chemical composition, size distribution, and hygroscopicity, all of

which are influenced by the emission sources and transformation and evolution

processes in the atmosphere.

The Yangtze River Delta (YRD) region is one of the most populated and

economically developed areas in China, but it is also facing with severe air pollution

lately. Nanjing, as one of the major megacities in this region, has a daily $PM_{2.5}$ mass

concentration varying between 33-234 μg m^{-3} during November 2011 - August 2012,

with an mean value of 106 μg m^{-3}, which is 4.2 times the WHO air quality standard of

25 μg m^{-3} (Shen et al., 2014). $PM_{2.5}$ pollution is significantly elevated during hazy

days, for example, a daily average of 282 μg m^{-3} was observed for a heavily polluted

day (Fu et al., 2008). A number of studies regarding aerosol chemistry in Nanjing

have been conducted, and identified various inorganic components (sulfate, nitrate,

ammonium and heavy metals, etc.) (e.g., Wang et al., 2003;Hu et al., 2012;Qi et al.,

2016) and hundreds of organic species (carboxylic/dicarboxylic acids, amines and

amino acids, polycyclic aromatic hydrocarbons, etc.) (Wang et al., 2011;Wang et al.,

87 2002;Yang et al., 2005;Wang et al., 2009) that contribute to the aerosol mass.

88 However, past studies mostly employed filter-based sampling technique, which due to

89 low time resolution (a few hours to days), is often incapable of capturing details of the

90 atmospheric evolution processes during the typical lifecycle of aerosols (Wexler and

91 Johnston, 2008). Subsequent offline analyses may also introduce artifacts as some

92 semi-volatile species can evaporate during sampling and storage (Dong et al., 2012).

93 On the other hand, in the past 15 years, the Aerodyne Aerosol Mass spectrometer

94 (AMS) (Canagaratna et al., 2007) has been widely used, and was proven to be

95 powerful for real-time online measurements of size-resolved chemical compositions

96 of submicron aerosols (PM_1) with very fine time resolution (seconds to minutes)

97 (Zhang et al., 2007a;Jimenez et al., 2009). The development of Aerodyne AMS began

98 with the invention of quadruple AMS (Q-AMS) (Jayne et al., 2000), following by the

99 compact time-of-flight AMS (C-ToF-AMS) (Drewnick et al., 2005), high resolution

100 time-of-flight AMS (HR-ToF-AMS) (DeCarlo et al., 2006) and the soot particle AMS

101 (SP-AMS) (Onasch et al., 2012). There are also an aerosol chemical speciation

102 monitor (ACSM) (Ng et al., 2011) and its updated version of ToF-ACSM (Fröhlich et

103 al., 2013), which are in particular designed for long-term unattended aerosol

104 measurements. SP-AMS is the most advanced version, which in principle incorporates

105 the single particle soot photometer (SP2) into the HR-ToF-AMS, and upgraded with a

106 laser vaporizer for detecting refractory black carbon (rBC) and associated/coated

107 species that cannot be measured by other types of AMS.

108 Recently, the Aerodyne AMS has been deployed widely in China (particularly

109 Beijing) (e.g., Xu et al., 2014 and references therein;Sun et al., 2014;Yeung et al.,

110 2014;Zhang et al., 2014;Li et al., 2015;Shen et al., 2015;Sun et al., 2015a;Sun et al.,

111 2015b;Yan et al., 2015;Zhang et al., 2015;Tang et al., 2016;Zhang et al., 2016a;Jiang

112 et al., 2015;Chen et al., 2015;Xu et al., 2015;Du et al., 2015;Sun et al., 2016;Wang et

113 al., 2015;Han et al., 2015;Wang et al., 2016b). However, only a few field campaigns

114 were conducted in the YRD region. Huang et al. (2012b) deployed an HR-ToF-AMS

115 together with an SP2 in Shanghai during the 2010 Shanghai World Expo, and in

Jiaxing during summer and winter of 2010 (Huang et al., 2012a). In urban Nanjing, an ACSM was applied for characterizing PM_1 during summer and autumn harvest seasons (Zhang et al., 2015), and during December 2013 to investigate a few heavy haze events (Zhang et al., 2016b). In addition, a Q-AMS was deployed in Nanjing to investigate the effects of PM_1 on visibility during January 2013 (Shen et al., 2015). Furthermore, a recent study by Wang et al. (2016a) reported the observation of fullerene soot in suburban Nanjing using an SP-AMS. Nevertheless, many questions remain unclear with regard to aerosol chemistry, sources, and processes in this region. Moreover, none of the previous AMS measurements studied the aerosol characteristics during springtime in Nanjing, yet the springtime aerosols may have different behaviors than those in other seasons, when aerosols are likely influenced significantly by emissions from biomass burning, coal burning etc. For these reasons, we reports in this work the real-time measurement results on urban fine aerosols in Nanjing using the SP-AMS during spring in 2015. The rich highly-time resolved, highly-chemical resolved mass spectral data, as well as chemically-resolved size distributions of different aerosol species obtained for the first time in Nanjing during this study, can allow us to conduct in-depth analyses, and better understand the characteristics, sources and relevant transformation processes of ambient aerosols. The findings for such a megacity are also valuable to the Pan-Eurasian Experiment (PEEX) infrastructure which aims to resolve the major uncertainties in Earth system science and global sustainability issues (Kulmala et al., 2015).

2. Experiments

2.1 Sampling site and instrumentation

The field campaign was conducted in the environment monitoring station of Nanjing Olympic center (32°0′33.00″N, 118°44′9.53″E, Fig. S1) from April 13 to 29, 2015. Details of the sampling site are shown in Fig. S1. The site was surrounded by residential buildings, close to a few urban arterial roads (~ 85 m northwest of Huangshan Road, ~ 200 m northeast to Mengdu Street and ~425 m southwest of

145   Xinglong Street). There are also a restaurant (~50 m), a student cafeteria (~300 m),

146   and the Nanjing Cigarette Factory (~480 m southeast) around the site.

147   The sampling inlet was installed outside the fifth floor of the building (~12 m

148   above the ground), with a $PM_{2.5}$ cyclone (URG Corp., Chapel Hill, NC, USA) to

149   remove coarse particles. Ambient particles were dried (RH <10%) via a diffusion

150   dryer filled with silica gel before entering into the SP-AMS. The sampling line (~2 m

151   long) was assembled using stainless steel tubing and proper fittings. Air flow was

152   controlled at around ~5 L min^{-1}, with a flow rate into the SP-AMS at ~80 cm^3 min^{-1}.

153   The SP-AMS can measure non-refractory (NR) PM_1 components including

154   ammonium, nitrate, sulfate, chloride and organics similar to other types of AMS via a

155   thermal tungsten heater. Moreover, it can also measure rBC and inorganic/organic

156   species that coated on the rBC cores, as it is equipped with an intracavity Nd:YAG

157   laser vaporizer (1064 nm) (Onasch et al., 2012). During this campaign, the instrument

158   was switched between "laser on" and "laser off" settings, and between V-mode (better

159   for mass quantification) and W-mode (better chemical resolution, ~5000 in this study),

160   with one cycle including six menu settings (M1: Laser on V-mode; M2: Laser off

161   V-mode; M3: Laser on W-mode; M4: Laser off W-mode; M7: Laser on PToF-mode;

162   M8: Laser off PToF-mode). Each menu was set to 2.5 min, thus a full running cycle

163   lasted for 15 mins. The PToF-mode was under V-mode, but was tuned in particular

164   for measuring particle sizes. The tungsten heater was always turned on and kept at

165   ~600$^{\text{o}}$C.

166   The SP-AMS, in conjunction with a scanning mobility particle sizer (SMPS) (TSI

167   inc., Shoreview, MN, USA) was calibrated for mass quantification (e.g., ionization

168   efficiency) using size-selected (250 nm and 300 nm) monodisperse ammonium nitrate

169   particles following the procedures detailed in Jimenez et al. (2003). Pure ammonium

170   sulfate was used to determine the relative ionization efficiency (RIE) of sulfate

171   (Setyan et al., 2012). Quantification of rBC was calibrated using Regal Black

172   (REGAL 400R pigment black, Cabot Corp.) particles according to the procedures

173   reported in Onasch et al. (2012). Note that the solution of Regal Black was sonicated

174 during calibration to maintain a relative stable aerosol flow. RIEs of ammonium,

175 nitrate, sulfate, chloride, organics and rBC were determined to be 3.15, 1.05, 1.20, 1.3,

176 1.4 and 0.33, respectively. On the other hand, particle sizing was calibrated using

177 standard polystyrene latex (PSL) spheres (Duke Scientific Corp., Palo Alto, CA, USA)

178 across 100 - 700 nm range. Flow rate was also calibrated prior to the measurement.

179   Concentrations of gaseous species, e.g., carbon monoxide (CO) (Model T300,

180 Teledyne API, USA), ozone (O_3) (Model EC9810, Ecotech Pty Ltd, Australia),

181 nitrogen dioxide (NO_2) and sulfur dioxide (SO_2) (Model LGH-01, Anhui Landun,

182 China), and meteorological data including air temperature (T), relative humidity (RH),

183 visibility (km), wind speed (WS) and wind direction (WD) were acquired at the same

184 site. $PM_{2.5}$ and PM_{10} mass concentrations were also recorded (BAM-1020, Met One

185 Instruments, Inc., USA), in parallel with the SP-AMS measurement.

186 2.2 Data treatment and source analyses

187   The SP-AMS data were post-processed by using the Igor-based standard

188 ToF-AMS Analysis Toolkit SQUIRREL v1.56D and PIKA v1.15D, available at:

189 http://cires1.colorado.edu/jimenez-group/ToFAMSResources/ToFSoftware/index.htm

190 l. Note all mass concentrations reported here were calculated from the HR fitted

191 results on V-mode data. A collection efficiency is typically used to account for the

192 particles that aren't collected and measured by the instrument, due to the particles lost

193 during passage through inlet, time-of-flight chamber and bouncing from the vaporizer.

194 For the SP-AMS, the CE of laser vaporizer is mainly governed by particle divergence,

195 while for the tungsten vaporizer, the CE is governed mainly by the bouncing effects

196 (Matthew et al., 2008). A CE value of 0.5 is valid and used commonly for the AMS

197 measurements for most environments (Canagaratna et al., 2007). Nevertheless,

198 Middlebrook et al. (2012) further investigated this issue, and found that high aerosol

199 acidity, high ammonium nitrate, and high sampling line RH can increase the CE, and

200 provide composition-dependent CE parametrization. For our dataset, we found that

201 the composition-dependent CE rather than a constant CE=0.5 has negligible effects on

202 the quantification of aerosol species, as the particles were neutralized (Fig. 3a), the

mass fraction of ammonium nitrate were <40% in almost all cases, and also the sampling line RH was below 10%. And in fact, the PM_1 mass concentrations quantified by using the composition-dependent CE correlate a bit worse with the $PM_{2.5}$ concentrations than ones using CE=0.5. Thus, we a constant CE of 0.5, in consistent with many other AMS studies, was employed for this dataset.

Unless specified, the concentrations of ammonium, sulfate, nitrate, chloride and organics are from M2 setting (tungsten vaporizer only), while the rBC data is from M1 setting (dual-vaporizers: tungsten + laser) in this paper. The meteorological data (RH, T, WS, WD and visibility), concentrations of gas-phase species (CO, NO_2, SO_2 and O_3) and $PM_{2.5}$ were averaged into hourly data for comparisons with the SP-AMS data. The data reported are at local time, e.g., Beijing (BJ) Time.

Positive matrix factorization (PMF) (Paatero and Tapper, 1994) was applied on the high resolution mass spectra (HRMS) of organic aerosol (OA) obtained under laser off W-mode (M4 setting) to elucidate the OA sources/processes. We used the PMF Evaluation Tool version 2.08A (downloaded from: http://cires1.colorado.edu/jimenez-group/wiki/index.php/PMF-AMS_Analysis_Guide) (Ulbrich et al., 2009) to investigate the PMF results by varying the number of factors (from 2 to 8 factors) and rotations ("$f$peak", from -1 to 1 with an increment of 0.1). Only ions with m/z less than or equal to 180 were included in the analyses. Following the instruction detailed by Zhang et al. (2011), the 4-factor solution (at $f$peak = -0.1) was chosen as the optimal solution, as the 3-factor solution cannot separate the hydrocarbon-like OA (HOA) and cooking OA (COA) (Fig. S2). For the 5-factor solution (Fig. S3), Factor 2 and Factor 4 are clearly a split from the SVOOA from the 4-factor solution ($r^2 = 0.89$ and slope of 1.05); Factor 2 of 5-factor solution also shows much weaker correlations with nitrate than SVOOA of 4-factor solution does ($r = 0.07$ vs. 0.49). A summary of the key diagnostic plots are provided in Fig. S4. Detailed discussion of the PMF results is presented in Section 3.5. Note we found no significant differences between the PMF source apportionment results from the HRMS of OA (without rBC) obtained with dual-vaporizers setting (M3 setting) and

232 current results (M4 setting, tungsten vaporizer only), as the OA HRMS acquired under

233 these two circumstances were overall very similar (details in Section 3.4).

234 Note the elemental ratios shown throughout the paper were all calculated based

235 on the method proposed by Aiken et al. (2008) (referred to as A-A method). Recently,

236 Canagaratna et al. (2015) improved this methodology by using specific ion fragments

237 as markers to calculate the O/C and H/C ratios (referred to as I-A method). The I-A

238 method increased the O/C ratio, H/C ratio, and the OM/OC ratio from the values

239 calculated from the A-A method, on average, by 28%, 10% and 8%, respectively (Fig.

240 S5). In this work, we used the results from the A-A method for consistency and

241 comparisons with previous AMS measurements.

242

243 **3. Results and discussion**

244 **3.1 Mass concentrations, chemical compositions and diurnal changes**

245 The temporal variations of meteorological parameters, concentrations of the gas

246 pollutants, concentrations and mass fractions of different PM_1 components, and the

247 $PM_{2.5}$ mass loadings (from Met one BAM-1020) over the sampling period are

248 illustrated in Fig. 1. During this study, the mean temperature was 18.5 ^{o}C, RH on

249 average was 64%, and wind predominantly blew from southeast and southwest (Fig.

250 S6). The SP-AMS PM_1 concentrations ranged from 5.1 to 97.9 µg m^{-3}, with an

251 average of 28.2 µg m^{-3}. Note this average PM_1 concentration is significantly lower

252 than those observed during summer (38.5 µg m^{-3}), autumn (46.4 µg m^{-3}) and winter

253 (89.3 µg m^{-3}) (Zhang et al., 2015;Zhang et al., 2016b), showing that the air during

254 springtime in Nanjing is cleaner than in other seasons. The variations of PM_1

255 concentrations also match very well with $PM_{2.5}$ concentrations (Pearson's $r^2 = 0.72$),

256 and on average PM_1 accounts for ~ 54% of the $PM_{2.5}$ mass. This ratio appears to be a

257 bit low, likely due to the uncertainty of CE of the SP-AMS.

258 The average PM_1 composition is shown in Fig. 2a. The most abundant component

259 is found to be organics (45.0%), following by sulfate (19.3%), nitrate (13.6%),

260 ammonium (11.1%), rBC (9.7%) and chloride (1.3%). Fig. 2b further shows changes

261 of the PM_1 chemical compositions in different concentration bins. It can be seen that

262 although most PM_1 mass loadings are within 10 - 40 µg m^{-3}, high loading periods tend

263 to have higher mass contributions from organics and rBC, and less contributions from

264 secondary inorganic species, indicating that high PM events were influenced

265 significantly by local fresh emissions.

266   The molar ratio of inorganic anions (sulfate, nitrate and chloride) to cations

267 (ammonium) is 1.05 (Fig. 3a) (Zhang et al., 2007b). Considering that a small fraction

268 of sulfate, nitrate and chloride are possibly associated with metal cations, such as Na^+,

269 K^+ and Ca^{2+}, etc., it can be concluded that the NR-PM_1 was overall neutral throughout

270 the study. On the other hand, the molar ratio of inorganic anions to ammonium is on

271 average 1.17 (Fig. 3b) when dual-vaporizers are on. This may be partially due to

272 variations of ionization/collection efficiencies of the measured species as the addition

273 of laser beam may change the distribution of vaporized species inside the ion chamber,

274 and also because of the detection of sulfate, nitrate and chloride bonded with metal

275 cations under the dual-vaporizers. These species don't evaporate on the tungsten

276 vaporizer under the laser-off mode. Indeed, more metal signals were observed with

277 the dual-vaporizers, as shown in Fig. S7.

278   Fig. 2c shows the average diurnal changes of organics, sulfate, nitrate, chloride

279 and rBC. Sulfate concentrations are slightly higher during daytime than during

280 nighttime, indicating a significant contribution from photochemical reactions. Sulfate

281 also shows the least variations among all species, reflecting its regional behavior.

282 Except for sulfate, all other species present a dual-peak pattern, with one peak in early

283 morning and another one in early evening. The peaks of rBC and organics are likely

284 due to local traffic/cooking activities (see details in Section 3.5), while the behavior of

285 nitrate is likely driven by the thermodynamic gas-particle partitioning: $NH_3(g)$ +

286 $HNO_3(g) \leftrightarrow NH_4NO_3(p)$ as it shows good anti-correlations with the diurnal changes

287 of temperatures ($r = -0.72$ for nitrate $vs.$ T). The good correlations between the diurnal

288 cycles of nitrate and RH, in particular during nighttime, suggest a nighttime formation

289 pathway of nitrate, e.g., $N_2O_5 + H_2O = 2HNO_3$ and $HNO_3 + NH_3 = NH_4NO_3$.

Furthermore, we calculated the diurnal variations of the equilibrium constant of NH$_4$NO$_3$ ($K_{p,AN}$) (Seinfeld and Pandis, 2006;Young et al., 2016) in Fig. 2c. The $K_{p,AN}$ displays a similar trend as nitrate ($r = 0.68$), providing strong evidence that nitrate variations were governed mainly by the thermodynamic equilibrium. Chloride shows similar behavior as nitrate, indicating it is driven by the equilibrium NH$_3$(g) + HCl(g) $\leftrightarrow$ NH$_4$Cl(p) as well ($r = -0.76$ for chloride *vs*. T). Therefore, when temperature rises, more NH$_4$NO$_3$ and NH$_4$Cl can dissociate into gaseous NH$_3$, HNO$_3$ and HCl, mass loadings of particle-phase nitrate and chloride decrease correspondingly, and *vice versa*.

In order to further elucidate the formation processes of sulfate, we calculated the oxidation ratios of sulfur (f_S) (Fig. 4a), defined as $f_S = nSO_4^{2-}/(nSO_4^{2-} + nSO_2)$ (Xu et al., 2014), indicating the conversion of SO$_2$. Here nSO_4^{2-} and nSO_2 are the molar quantities of particle-phase sulfate, and gas-phase SO$_2$, respectively. Diurnal variations of f_S and RH are presented in Fig.4b, and Fig. 4c shows variations of sulfate and nitrate concentrations with RH. The diurnal profile of f_S shows a negative correlation with that of RH ($r = -0.52$), and mass concentrations of sulfate even drop under high RH conditions, indicating an insignificant role of aqueous-phase processing for sulfate formation during this campaign. On the other hand, the f_S reaches a maximum around 3 pm. Note the afternoon rise of fs and sulfate may be affected by the down mixing of sulfate formed earlier, however, since concentrations of all other aerosol species that mix with sulfate decrease significantly, we postulate that the increase of fs likely suggest the photochemical production of sulfate in the afternoon.

3.2 Chemically-resolved size distributions

The campaign-averaged mass-based size distributions, fractional contributions and diurnal size distributions (image plots) of the major PM$_1$ species are depicted in Fig. 5 (temporal variations of the mass-based size distributions of these PM$_1$ species over the whole measurement period are provided in Fig. S8). Note the size

319   distribution of rBC in these plots were scaled from the size distribution of m/z 24

320   (C_2^+), as other major rBC ion clusters may be heavily influenced by other ions, such

321   as C^+ signal but from organics at m/z 12 (C^+), HCl^+ signal at m/z 36 (C_3^+), SO^+ signal

322   at m/z 48 (C_4^+), $C_2H_4O_2^+$ signal at m/z 60 (C_5^+). It also should be note that, although

323   the AMS is able to capture the bulk of atmospheric accumulation mode particles

324   (Canagaratna et al., 2007), right side of size distributions may be affected by the

325   incomplete transmission of larger particles limited by the SP-AMS inlet (in particular,

326   the supermicron ones).

327   As can be expected, all inorganic species (sulfate, nitrate, chloride and

328   ammonium) display a unimodal distribution with an accumulation mode peaking

329   ~550 nm (vacuum aerodynamic diameter, D_{va} (DeCarlo et al., 2004)), since they were

330   mainly formed from secondary reactions. The organics has a much broader size

331   distribution across from ultrafine (<100 nm) to supermicron meter range, with a small

332   sub-peak centering ~120 nm in addition to the major peak at ~440 nm, indicating

333   influences from both primary and secondary emissions. On the contrary, size

334   distribution of rBC behaves very differently from other components, which peaks at

335   90 - 200 nm range, reflecting clearly that it is mainly originated from primary

336   emissions. Overall, the small particles are predominantly consisted of organics and

337   rBC, which together account for more than 90% of the ultrafine particle mass. Mass

338   contributions from inorganic species increase significantly with the increase of

339   particle size, and they dominate masses of particles larger than 400 nm (Fig. 5b).

340   In line with the diurnal mass loadings of the PM_1 species shown in Fig. 2c, the

341   diurnal size distribution of sulfate is generally stable, with masses concentrating in the

342   400 - 700 nm range throughout the day (Fig. 5c); while the size distributions of nitrate,

343   chloride and organics present clear enhancements in the 300 - 700 nm range during

344   early morning and early evening due to increased mass concentrations of these species

345   during these two periods. The size distribution of rBC is also enhanced during the

346   morning and evening hours, but it extends to a much smaller size range (<100 nm).

347

348 **3.3 PM$_1$ contributions on visibility impairment**

349   In order to figure out the major species that are responsible for the visibility

350 degradation, here we employed the IMPROVE method to reconstruct the light

351 extinction coefficients (b_{ext}). b_{ext} values are derived from the measured visibility:

352 b_{ext}=3.91/V_s (Kong et al., 2015), where V_s stands for the visibility (in meter). The

353 following IMPROVE formula (Yang et al., 2007) was used:

354   b_{ext} = 3f(RH){[(NH$_4$)$_2$SO$_4$] + [NH$_4$NO$_3$] + [NH$_4$Cl]} + 4[OM] + 10[BC] + 1[soil]+10

355 Where f(RH) is a RH-dependent empirical coefficient which considers the effects of

356 water uptake by inorganic salts on the light extinction; the f(RH) values used here

357 were taken from Malm and Day (2001), which were regressed from the Great Smoky

358 data set. [(NH$_4$)$_2$SO$_4$], [NH$_4$NO$_3$], [NH$_4$Cl], [OM], and [BC] represent the mass

359 concentrations of ammonium sulfate, ammonium nitrate, ammonium chloride,

360 organics and black carbon directly from the SP-AMS measurements (in μg m^{-3})

361 ([(NH$_4$)$_2$SO$_4$] = 1.375*[SO$_4^{2-}$], [NH$_4$NO$_3$]=1.29*[NO$_3^-$] and [NH$_4$Cl] = 1.51*[Cl$^-$]).

362 Since the SP-AMS cannot accurately measure soil components (e.g., various

363 metals/metal oxides/metal salts), the term [soil] was set to zero during calculations.

364   By using this method, the reconstructed visibilities match reasonably well with

365 the measured values (r^2 = 0.50) as shown in Fig. 6a. Fig. 6b shows the time series of

366 the measured and reconstructed extinction coefficients throughout the whole sampling

367 period. It should be noted that, on average, the measured PM$_1$ species are only able to

368 explain ~44% of the light extinction. This is likely due to that: 1) as shown earlier, the

369 SP-AMS measured PM$_1$ only occupies ~54% of the PM$_{2.5}$ mass; 2) we didn't include

370 contributions from soil components, coarse particles and also some gas-phase species

371 (such as NO$_2$); 3) although the influences of water are included in part through f(RH)

372 for inorganic salts, the water uptake by organic species are not considered explicitly,

373 which can be significant especially for the SOA under high RH conditions (Duplissy

374 et al., 2011;Denjean et al., 2015). Indeed, as shown in Fig. 6a, reconstructed

375 visibilities appear to deviate more significantly from the measured visibilities under

376 high RH than ones under low RH conditions, suggesting the importance of

377 particle-bounded water on visibility degradation. The pie chart in Fig. 6b presents the

378 average relative contributions of different components to the light extinction of PM_1.

379 The largest contributor is organics which accounts for 37.7%, followed by ammonium

380 sulfate (25.1%), rBC (20.7%), ammonium nitrate (15.1%) and a minor contributor of

381 ammonium chloride (1.4%).

382

383 **3.4 Chemical characteristics of OA**

384   The unique laser vaporizer of SP-AMS allows it to detect rBC and species coated

385 on the rBC core including both non-refractory and refractory organics, thus

386 comparison between the OA mass spectra obtained with dual-vaporizers and tungsten

387 vaporizer settings, can infer some information regarding the chemical features of

388 refractory organics, which were unable to be determined by any other types of AMS.

389 As shown in Fig. 7a and 7b, the OA obtained with dual-vaporizers setting have

390 slightly higher oxygen-to-carbon (O/C) ratio (0.28 $vs.$ 0.27), nitrogen-to-carbon (N/C)

391 ratio (0.033 $vs.$ 0.032) and lower hydrogen-to-carbon (H/C) ratio (1.50 $vs.$ 1.52) than

392 the corresponding elemental ratios of OA obtained with the tungsten vaporizer only.

393 This result indicates that refractory organics are likely more oxygenated than the

394 non-refractory organics, and for this dataset it is mainly due to a higher fractional

395 contribution from $C_2H_3O^+$ (see the inset of Fig. 7a). This is different from the results

396 on laboratory-generated nascent soot, where larger fCO_2^+ (i.e., the fraction of total

397 organic signal contributed by CO_2^+) was observed with the dual-vaporizers setting,

398 indicating the variability of the chemical compositions of refractory organics.

399   It should be noted that, accurate determination of refractory organics is very

400 difficult, because: 1) A large portion of refractory organics cannot be detected by the

401 SP-AMS if they didn't coat on rBC cores; 2) To accurately measure the species only

402 coated on rBC cores, the tungsten vaporizer has to be physically removed, otherwise

403 the vaporizer temperature is still around 150^oC even its power is turned off, and the

404 non-refractory organics that don't coat on rBC cores can still be measured, and

405 complicates the analyses; 3) The CE and IE values for different species may vary

under different vaporizer settings, so that direct subtraction of organics measured under tungsten-only setting from the organics measured under dual-vaporizer setting may not represent the real refractory organics; 4) Some ions measured under dual-vaporizer setting are likely induced by the laser itself rather than the 70 ev electron impact. For example, a series of fullerene-like carbon clusters can be generated by the laser itself, even though they don't really exist in the atmosphere (Wang et al., 2016a;Onasch et al., 2015). This laser-induced ion formation scheme may work for other organics, thus makes it even more difficult for identifying the refractory organics. Further studies are essential to investigate this issue.

Overall, the O/C ratio (0.27) of OA in Nanjing during springtime is a bit lower than those observed at other urban locations in China – for instances, 0.30 in Shenzhen (He et al., 2011), 0.31 in Shanghai (Huang et al., 2012b), 0.33 in Lanzhou (Xu et al., 2014) and 0.34 in Beijing (Zhang et al., 2014), and much lower than those at rural sites – for instances, 0.47 in Kaiping (Huang et al., 2011) and 0.59 in Changdao (Hu et al., 2013). As O/C ratio is a good indicator of the aging degree of OA, the relatively low O/C level indicates a significant contribution from fresh emissions in Nanjing aerosols during springtime. Accordingly, the non-refractory OA (pie chart in Fig. 7b) is dominated in hydrocarbon $C_xH_y^+$ ions (51.2%) rather than the oxygen-containing ion fragments (37.4% of $C_xH_yO_1^+$ and $C_xH_yO_2^+$).

The scatter plot of $f44$ (mass fraction of m/z 44 to the total OA) $vs.$ $f43$ (mass fraction of m/z 43 to the total OA) (a.k.a., triangle plot) (Ng et al., 2010) was often used to investigate the oxidation degrees of OA. As presented in Fig. 8, most OA reside in the bottom end of the triangular region, again pointing out the less-oxygenated behavior of the OA. Since the HRMS can separate different ions at the nominal m/z, we also examined the fCO_2^+ $vs.$ $fC_2H_3O^+$ space and illustrated it in Fig. S9 - many OA locate outside the triangular region, yet still close to the bottom. Moreover, m/z 60 (mainly $C_2H_4O_2^+$) is a significant fragment ion of levoglucosan, which is well known as the biomass burning aerosol tracer (Alfarra et al., 2007). However, as $f60$ (mass fraction of m/z 60 to the total OA) is very low in OA (average

435 ± 1σ = 0.4 ± 0.06 %), indicating no biomass burning influences on the OA properties

436 during springtime in Nanjing.

437

3.5 Sources and evolution processes of OA

439 In order to further elucidate the sources and evolution processes of OA, we

440 performed PMF analyses and identified four OA components, including two primary

441 OA (POA) factors – a traffic-related hydrocarbon-like OA (HOA) and a

442 cooking-related OA (COA), and two secondary OA factors – a semi-volatile

443 oxygenated OA (SV-OOA) and a low volatility OOA (LV-OOA). Details about their

444 characteristics are discussed below.

3.5.1 Mass spectral features of the OA factors

446 The mass spectral profiles, time-dependent mass concentrations of the four OA

447 factors and corresponding tracer ions are presented in Fig. 9. The HOA mass spectrum

448 is overall dominated by the $C_xH_y^+$ ions (73.2%), such as $C_3H_7^+$, $C_4H_7^+$, $C_4H_9^+$, $C_5H_9^+$

449 etc., which are most likely produced from alkanes and cycloalkanes emitted from fuel

450 and lubricating oil burning (Canagaratna et al., 2004). This feature is in good

451 agreement with the mass spectral features of POA directly from vehicle

452 emissions(Collier et al., 2015), and the HOA factors determined in many other

453 locations (e.g., Ge et al., 2012b;Huang et al., 2010;Sun et al., 2011). HOA has the

454 lowest O/C ratio (0.10) and highest H/C ratio (1.75) among all factors, representing its

455 behavior as primary fresh emissions. The COA mass spectrum is also rich in $C_xH_y^+$

456 ions (64.7%), but having more oxygenated ions ($C_xH_yO_z^+$) than the HOA (26.5% *vs*.

457 15.4%), especially $C_3H_3O^+$ and $C_3H_5O^+$ ions. The significant contributions of $C_3H_3O^+$

458 and $C_3H_5O^+$ to *m/z* 55 and *m/z* 57 are a common feature of COA, that has been

459 reported in various urban locations around the world, for examples, Beijing (Sun et al.,

460 2015a), London (Allan et al., 2010), Fresno (Ge et al., 2012b), New York City (Sun et

461 al., 2011) and Barcelona (Mohr et al., 2012;Mohr et al., 2015). These

462 oxygen-containing ions are in part generated from the fragmentation of fatty acids in

463 the cooking aerosols (Ge et al., 2012b). As a result, COA has a higher O/C ratio of

464 0.16 and a lower H/C ratio of 1.67 than those of HOA. The O/C and H/C levels of

465 COA in this work are also close to those identified in other locations aforementioned.

466 The consistency of the chemical characteristics of COA from such different locations

467 suggests that ambient COA is more relevant to the cooking oil rather than the different

468 types of food, which was postulated earlier by Allan et al. (2010).

469   Unlike the two POA factors, SV-OOA and LV-OOA are both abundant in

470 oxygen-containing fragments ($C_xH_yO_z^+$ ions), which are 46.4% and 54.8%,

471 respectively. The higher O/C ratio (0.55 *vs.* 0.32) and more $C_xH_yO_2^+$ ions (18.8% *vs.*

472 11.8%) in the LV-OOA mass spectrum than those of the SV-OOA, reflecting the fact

473 that LV-OOA went through more aging/oxidation reactions than SV-OOA. The O/C

474 ratio of SV-OOA is 0.32, which is within the O/C range of SV-OOA observed

475 worldwide (Jimenez et al., 2009). The LV-OOA O/C ratio of 0.55 is in the lower end

476 compared to the O/C levels of LV-OOA observed in other China sites, for examples,

477 0.64 in Kaiping (Huang et al., 2011), 0.65 in Shanghai (Huang et al., 2012b), 0.68 in

478 Lanzhou (Xu et al., 2014), 0.78 in Changdao (Hu et al., 2013) and 0.80 in Hong Kong

479 (Lee et al., 2013).

480   Consistently, in the *f*44 *vs.* *f*43 space (Fig. 8), SV-OOA situates near the bottom

481 side while LV-OOA approaches to the upper part of the triangular region, because of a

482 much larger fractional contribution of CO_2^+ in the LV-OOA mass spectrum. HOA and

483 COA, as POA factors, both reside in the bottom end of the plot, away from SV-OOA

484 and LV-OOA; while they locate outside the triangle in the *f*CO_2^+ *vs.* *f*$C_2H_3O^+$ space

485 (Fig. S9), indicating that the HRMS acquired by the SP-AMS is better in

486 differentiating POA factors from other SOA factors than the unit mass resolution

487 (UMR) data.

488   In order to justify the OA factors identified in this study, we compared the

489 spectral similarities of the OA factor spectral profiles (in both HR and UMR) with

490 those separated during wintertime in Beijing (Sun et al., 2015a), summertime in

491 Lanzhou (Xu et al., 2014), and wintertime in Fresno (Ge et al., 2012b;Ge et al.,

492 2012a). The results are listed in Table 1. Indeed, the HOA, COA and LV-OOA mass

493 spectra are highly similar to the corresponding factors identified in Bejing, Lanzhou

494 and Fresno ($r^2 > 0.87$); SV-OOA also correlates fairly well with Bejing and Lanzhou

495 SV-OOA too, but with relative low r^2 (0.68 – 0.75), mainly because of one or two ion

496 fragments, namely, higher CO^+ and CO_2^+ signals in Beijing SV-OOA and higher

497 $C_2H_3O^+$ signal in Lanzhou SV-OOA than those in Nanjing SV-OOA. The SV-OOA on

498 the other hand, correlates very well with the Fresno OOA ($r^2 = 0.90$ and 0.91).

499   Moreover, as presented in Fig. 9a, the HOA mass spectrum contains relatively

500 higher fraction of ions with large m/z values ($m/z > 100$) than that of COA (14.0% *vs.*

501 8.2%), and most of these ions are $C_xH_y^+$ ions, probably from fuel burning emitted

502 long-chain alkanes, etc. The SV-OOA also includes more large m/z ion fragments ($m/z >$

503 100) than those in the LV-OOA mass spectrum (10.5% *vs.* 5.3%), likely suggesting

504 that further oxidation of SOA species may lead to the fragmentation of high molecular

505 weight species and formation of small molecules – a mechanism verified by both

506 lab-scale experiments (e.g., Yu et al., 2014) and field measurements (e.g., Lee et al.,

507 2012).

3.5.2 Temporal variations, diurnal patterns and relative contributions of the OA

factors

510   The temporal variations of different OA factors and their corresponding tracer

511 ions are displayed in Fig. 9b. $C_4H_9^+$ ion, a.k.a., the HOA mass spectral tracer (Zhang

512 et al., 2005) indeed varies very closely to the HOA ($r^2 = 0.94$). Time series of the COA

513 tracer ion $C_6H_{10}O^+$ (and also $C_5H_8O^+$, $C_7H_{12}O^+$) (Sun et al., 2011;Ge et al., 2012b)

514 match very well with that of COA too ($r^2 = 0.90$). SV-OOA correlates better with

515 $C_2H_3O^+$ ($r^2 = 0.90$) than with CO_2^+ ($r^2 = 0.66$). Although LV-OOA doesn't correlate

516 very well with CO_2^+ ($r^2 = 0.12$) mainly due to the mismatch during April 23 - 26, the

517 correlation is still much better than it with $C_2H_3O^+$ ($r^2 < 0.001$). In Table 2, we

518 tabulate the correlation coefficients (r) of the four OA factors with the gas-phase

519 species, BC and inorganic species. Note we used Pearson's r not r^2 here since some

520 correlation coefficients are negative. From the table, it is clear that the traffic-related

521 gaseous species, CO and NO_2, correlate best with HOA among all OA factors;

522   SV-OOA correlates better with nitrate ($r = 0.49$) than it with sulfate ($r = 0.11$);

523   LV-OOA correlate better with sulfate ($r = 0.23$) that it with nitrate ($r = 0.11$). All these

524   results are consistent with the traffic origin of HOA, the semi-volatile and

525   low-volatility behaviors of SV-OOA and LV-OOA.

526   Accordingly, diurnal cycles of the OA factors are presented in Fig. 10a.

527   Correlation coefficients (r) of the diurnal variations between OA factors with

528   gas-phases and inorganic species are provided in Table 2, as well. HOA

529   concentrations show an early morning peak, and it overall remains at high levels

530   during nighttime. Besides the impacts of boundary layer height, this is also due to

531   enhanced emissions from construction vehicles around the site, which were in fact

532   much more active during nighttime than during daytime because of the restrictions of

533   Nanjing government. Most of those vehicles used low-quality diesel fuel, and could

534   emit a large amount of rBC particles. The rBC diurnal pattern is indeed almost

535   identical to that of HOA ($r =0.99$), indicating that the HOA during this campaign was

536   apparently associated with the construction vehicle emissions. COA concentrations

537   increase during noon (12 pm – 1 pm) and early evening, in response to the lunchtime

538   and dinnertime cooking activities. SV-OOA concentrations decreases from 9 am, and

539   reach a minimum during afternoon (3 pm – 4 pm), oppositely to the variation of

540   temperatures ($r = -0.85$) but similar to that of nitrate ($r = 0.53$), corroborating its

541   semi-volatile feature. Different from other factors, LV-OOA concentrations increase

542   during daytime and shows positive correlation with temperature ($r = 0.76$); it also has

543   negative correlation with the diurnal cycle of RH ($r = -0.75$). Both behaviors are

544   similar to those of sulfate ($r = 0.72$ for the diurnal cycle of LV-OOA *vs.* sulfate),

545   indicating the leading role of photochemical oxidation for LV-OOA formation as well.

546   As shown in Fig. 10b, due to mainly the increase of LV-OOA mass loading, OA is

547   overwhelmingly dominated by the SOA (SV-OOA + LV-OOA) during afternoon (80.2%

548   at 3 pm); POA (HOA + COA) only dominates the OA mass during morning (53.2% at

549   7 am) and early evening (56.9% at 8 pm) in response to the enhanced traffic and

550   cooking emissions. On average, the OA is composed of 27.6% of HOA, 16.9% of

COA, 27.4% of SV-OOA and 28.1% of LV-OOA (Fig. 10c), with SOA outweighing

POA (55.5% *vs.* 44.5%). However, as shown in Fig. 10d, with the increase of OA

mass loadings, the fractional contribution of POA increases, highlighting the

important and direct influences of anthropogenic emissions on the heavy pollution

haze events.

3.5.3 Local/regional influences and evolution processes of the OA factors

Combining WS, WD and mass loadings, the bivariate polar plots of the four OA

factors, rBC, total OA, nitrate, sulfate and the total PM_1 are shown in Fig. 11. These

plots provide an effective graphical method for showing the potential influences of air

masses from different directions with different wind speeds to the receptor site

(Carslaw and Beevers, 2013). Clearly, high mass loadings of HOA and rBC mostly

link with low WS (< 1 m s^{-1}), indicating they are mainly from local vehicle emissions.

High COA concentrations occur mainly under low WS as well, but with some high

concentrations accompanied with air masses from southeast under higher WS.

SV-OOA appears to be mainly formed locally, except for a concentration hotspot in

the southeast – likely due to emissions from the tobacco factory that resides in that

direction. Nitrate, as a semi-volatile species, behaves overall similar to the SV-OOA.

High concentrations of LV-OOA are distributed in all directions under higher WS,

similar to that of sulfate, representing their regional behaviors. Overall, high PM_1

mass loadings occur mainly under low WS, indicating that the PM_1 is heavily affected

by local emissions rather than pollutants in a regional scale.

The aging of OA can be described in general by the increase of O/C and decrease

of H/C. In this regard, we plotted the Van Krevelen diagram (Heald et al., 2010) (Fig.

12a) to show the relationships between H/C and O/C ratios for all OA as well as the

four OA factors. Overall, in this study, the H/C and O/C ratios of OA data are

correlated linearly with a slope of -1.04 ($r^2 = 0.93$). Interestingly, the two OOA factors

lie very well on the fitted straight line. This trend may suggest that the evolution of

secondary OA during this campaign follows a transformation pathway of SV-OOA to

580   LV-OOA. The diurnal cycle of LV-OOA varies oppositely to that of SV-OOA ($r =$

581   -0.86), probably supporting this hypothesis. In addition, SV-OOA and LV-OOA mass

582   concentrations, and O/C ratios of OA all show no obvious correlations with the RH as

583   shown in Fig. 12b and Fig. 12c, indicating that aqueous-phase processing is

584   insignificant compared to the photochemical processing for the oxidation of OA.

585

4. Conclusions

587   We present for the first time the real-time measurement results using the SP-AMS

588   on submicron aerosols in urban Nanjing during springtime (April 13 - 29, 2015). The

589   dynamic variations of SP-AMS determined PM_1 mass loadings, agreed well with the

590     $PM_{2.5}$ measured by the Met One $PM_{2.5}$ analyzer. The average PM_1 concentration was

591   28.2 μg m^{-3}, lower than previously ACSM-determined PM_1 concentrations during

592   summer and winter in Nanjing. Organics on average comprised the largest fraction

593   (45%) of PM_1, and its fractional contributions increased in case of high PM_1 mass

594   loadings. The diurnal cycles of mass concentrations of organics, rBC, nitrate and

595   chloride all presented a similar behavior, which was high in early morning and

596   evening, but low in the afternoon. Concentrations of sulfate, on the contrary, increased

597   during afternoon. Further investigations of f_S, sulfate concentrations and its

598   relationship with RH suggest that photochemical processing contributed significantly

599   to sulfate formation compared to the aqueous-phase processing, while nitrate (and

600   chloride) formation was mainly governed by the thermodynamic equilibrium. The

601   chemically-resolved mass-based size distribution data showed that rBC occupied a

602   large fraction of ultrafine particles, while secondary inorganic species could dominate

603   the mass of particles larger than 400 nm (D_{va}). In addition, by using the IMPROVE

604   method, we found that the observed PM_1 components were able to reproduce ~44% of

605   the light extinction during this study.

606   PMF analyses resolved four OA factors, e.g., HOA, COA, SV-OOA and LV-OOA.

607   Mass spectral profiles of these factors agree very well with the corresponding factors

608   identified at other locations. The springtime OA showed no influences from biomass

609 burning emissions. On average, the OA is dominated by SOA (55.5%), but POA

610 appeared to be more important when the OA mass loadings are high, and can be

611 dominant in early morning and evening. Diurnal cycle of SV-OOA varied similarly to

612 that of nitrate, reflecting its semi-volatile behavior. Diurnal variations of LV-OOA

613 showed great resemblance to that of sulfate. The bivariate polar plots indicate that

614 SV-OOA was formed locally, and the Van Krevelen diagram further suggests a

615 transformation from SV-OOA to LV-OOA in Nanjing. Generally, our highly

616 time-resolved SP-AMS measurement results may offer useful insights into the aerosol

617 chemistry, and have important implications for the PM control and reduction in this

618 densely populated region.

619

620 **Acknowledgements**

621 This work was supported by the Natural Science Foundation of China (Grant Nos.

622 21407079 and 91544220), the Jiangsu Natural Science Foundation (BK20150042),

623 the Jiangsu Provincial Specially-Appointed Professors Foundation, the LAPC Open

624 Fund (LAPC-KF-2014-06), and the project funded by the Priority Academic Program

625 Development of Jiangsu Higher Education Institutions (PAPD). M. Chen

626 acknowledges the support from the Natural Science Foundation of China (Grant Nos.

627 21577065 and 91543115), the Commonweal Program of Environment Protection

628 Department of China (201409027-05), and the International ST Cooperation Program

629 of China (2014DFA90780). J. Wang also acknowledges the financial support from

630 China Scholarship Council, and the innovative project for graduate student of Jiangsu

631 Province. The authors thank Nanjing Environmental Monitoring Center for the

632 supporting data, and the helps from Ling Li, Yanan He, Hui Chen and Yangzhou Wu

633 during the campaign and preparation of the manuscript.

634

References

Aiken, A. C., Decarlo, P. F., Kroll, J. H., Worsnop, D. R., Huffman, J. A., Docherty, K. S., Ulbrich, I. M., Mohr, C., Kimmel, J. R., Sueper, D., Sun, Y., Zhang, Q., Trimborn, A., Northway, M., Ziemann, P. J., Canagaratna, M. R., Onasch, T. B., Alfarra, M. R., Prevot, A. S. H., Dommen, J., Duplissy, J., Metzger, A., Baltensperger, U., and Jimenez, J. L.: O/C and OM/OC ratios of primary, secondary, and ambient organic aerosols with high-resolution time-of-flight aerosol mass spectrometry, Environ. Sci. Technol., 42, 4478-4485, 10.1021/Es703009q, 2008.

Alfarra, M. R., Prevot, A. S. H., Szidat, S., Sandradewi, J., Weimer, S., Lanz, V. A., Schreiber, D., Mohr, M., and Baltensperger, U.: Identification of the Mass Spectral Signature of Organic Aerosols from Wood Burning Emissions, Environ. Sci. Technol., 41, 5770-5777, 10.1021/es062289b, 2007.

Allan, J. D., Williams, P. I., Morgan, W. T., Martin, C. L., Flynn, M. J., Lee, J., Nemitz, E., Phillips, G. J., Gallagher, M. W., and Coe, H.: Contributions from transport, solid fuel burning and cooking to primary organic aerosols in two UK cities, Atmos. Chem. Phys., 10, 647-668, 10.5194/acp-10-647-2010, 2010.

Canagaratna, M. R., Jayne, J. T., Ghertner, D. A., Herndon, S., Shi, Q., Jimenez, J. L., Silva, P. J., Williams, P., Lanni, T., Drewnick, F., Demerjian, K. L., Kolb, C. E., and Worsnop, D. R.: Chase studies of particulate emissions from in-use New York City vehicles, Aerosol Sci. Tech., 38, 555-573, 10.1080/02786820490465504, 2004.

Canagaratna, M. R., Jayne, J. T., Jimenez, J. L., Allan, J. D., Alfarra, M. R., Zhang, Q., Onasch, T. B., Drewnick, F., Coe, H., Middlebrook, A., Delia, A., Williams, L. R., Trimborn, A. M., Northway, M. J., DeCarlo, P. F., Kolb, C. E., Davidovits, P., and Worsnop, D. R.: Chemical and microphysical characterization of ambient aerosols with the aerodyne aerosol mass spectrometer, Mass Spectrom. Rev., 26, 185-222, 10.1002/Mas.20115, 2007.

Canagaratna, M. R., Jimenez, J. L., Kroll, J. H., Chen, Q., Kessler, S. H., Massoli, P., Hildebrandt Ruiz, L., Fortner, E., Williams, L. R., Wilson, K. R., Surratt, J. D., Donahue, N. M., Jayne, J. T., and Worsnop, D. R.: Elemental ratio measurements of organic compounds using aerosol mass spectrometry: characterization, improved calibration, and implications, Atmos. Chem. Phys., 15, 253-272, 10.5194/acp-15-253-2015, 2015.

Cao, J. J., Xu, H. M., Xu, Q., Chen, B. H., and Kan, H. D.: Fine Particulate Matter Constituents and Cardiopulmonary Mortality in a Heavily Polluted Chinese City, Environ. Health Persp., 120, 373-378, 10.1289/ehp.1103671, 2012.

Carslaw, D. C., and Beevers, S. D.: Characterising and understanding emission sources using bivariate polar plots and k-means clustering, Environ. Model. Soft., 40, 325-329, 10.1016/j.envsoft.2012.09.005, 2013.

Carslaw, K. S., Boucher, O., Spracklen, D. V., Mann, G. W., Rae, J. G. L., Woodward, S., and

672   Kulmala, M.: A review of natural aerosol interactions and feedbacks within the Earth system,
673   Atmos. Chem. Phys., 10, 1701-1737, 10.5194/acp-10-1701-2010, 2010.

674   Chen, C., Sun, Y. L., Xu, W. Q., Du, W., Zhou, L. B., Han, T. T., Wang, Q. Q., Fu, P. Q., Wang,
675   Z. F., Gao, Z. Q., Zhang, Q., and Worsnop, D. R.: Characteristics and sources of submicron
676   aerosols above the urban canopy (260 m) in Beijing, China, during the 2014 APEC summit,
677   Atmos. Chem. Phys., 15, 12879-12895, 10.5194/acp-15-12879-2015, 2015.

678   Collier, S., Zhou, S., Kuwayama, T., Forestieri, S., Brady, J., Zhang, M., Kleeman, M., Cappa,
679   C., Bertram, T., and Zhang, Q.: Organic PM Emissions from Vehicles: Composition, O/C
680   Ratio, and Dependence on PM Concentration, Aerosol Sci. Tech., 49, 86-97,
681   10.1080/02786826.2014.1003364, 2015.

682   DeCarlo, P. F., Slowik, J. G., Worsnop, D. R., Davidovits, P., and Jimenez, J. L.: Particle
683   morphology and density characterization by combined mobility and aerodynamic diameter
684   measurements. Part 1: Theory, Aerosol Sci. Tech., 38, 1185-1205,
685   10.1080/02786820590928897, 2004.

686   DeCarlo, P. F., Kimmel, J. R., Trimborn, A., Northway, M. J., Jayne, J. T., Aiken, A. C., Gonin,
687   M., Fuhrer, K., Horvath, T., Docherty, K. S., Worsnop, D. R., and Jimenez, J. L.:
688   Field-deployable, high-resolution, time-of-flight aerosol mass spectrometer, Anal. Chem., 78,
689   8281-8289, 10.1021/Ac061249n, 2006.

690   Denjean, C., Formenti, P., Picquet-Varrault, B., Pangui, E., Zapf, P., Katrib, Y., Giorio, C.,
691   Tapparo, A., Monod, A., Temime-Roussel, B., Decorse, P., Mangeney, C., and Doussin, J. F.:
692   Relating hygroscopicity and optical properties to chemical composition and structure of
693   secondary organic aerosol particles generated from the ozonolysis of α-pinene, Atmos. Chem.
694   Phys., 15, 3339-3358, 10.5194/acp-15-3339-2015, 2015.

695   Dong, H. B., Zeng, L. M., Hu, M., Wu, Y. S., Zhang, Y. H., Slanina, J., Zheng, M., Wang, Z.
696   F., and Jansen, R.: Technical Note: The application of an improved gas and aerosol collector
697   for ambient air pollutants in China, Atmos. Chem. Phys., 12, 10519-10533,
698   10.5194/acp-12-10519-2012, 2012.

699   Drewnick, F., Hings, S. S., DeCarlo, P., Jayne, J. T., Gonin, M., Fuhrer, K., Weimer, S.,
700   Jimenez, J. L., Demerjian, K. L., Borrmann, S., and Worsnop, D. R.: A new time-of-flight
701   aerosol mass spectrometer (TOF-AMS) - Instrument description and first field deployment,
702   Aerosol Sci. Tech., 39, 637-658, 10.1080/02786820500182040, 2005.

703   Du, W., Sun, Y. L., Xu, Y. S., Jiang, Q., Wang, Q. Q., Yang, W., Wang, F., Bai, Z. P., Zhao, X.
704   D., and Yang, Y. C.: Chemical characterization of submicron aerosol and particle growth
705   events at a national background site (3295 m a.s.l.) on the Tibetan Plateau, Atmos. Chem.
706   Phys., 15, 10811-10824, 10.5194/acp-15-10811-2015, 2015.

707   Duplissy, J., DeCarlo, P. F., Dommen, J., Alfarra, M. R., Metzger, A., Barmpadimos, I., Prevot,
708   A. S. H., Weingartner, E., Tritscher, T., Gysel, M., Aiken, A. C., Jimenez, J. L., Canagaratna,

M. R., Worsnop, D. R., Collins, D. R., Tomlinson, J., and Baltensperger, U.: Relating hygroscopicity and composition of organic aerosol particulate matter, Atmos. Chem. Phys., 11, 1155-1165, 10.5194/acp-11-1155-2011, 2011.

Fröhlich, R., Cubison, M. J., Slowik, J. G., Bukowiecki, N., Prévôt, A. S. H., Baltensperger, U., Schneider, J., Kimmel, J. R., Gonin, M., Rohner, U., Worsnop, D. R., and Jayne, J. T.: The ToF-ACSM: a portable aerosol chemical speciation monitor with TOFMS detection, Atmos. Meas. Tech., 6, 3225-3241, 10.5194/amt-6-3225-2013, 2013.

Fu, Q. Y., Zhuang, G. S., Wang, J., Xu, C., Huang, K., Li, J., Hou, B., Lu, T., and Streets, D. G.: Mechanism of formation of the heaviest pollution episode ever recorded in the Yangtze River Delta, China, Atmos. Environ., 42, 2023-2036, 10.1016/j.atmosenv.2007.12.002, 2008.

Ge, X., Zhang, Q., Sun, Y., Ruehl, C. R., and Setyan, A.: Effect of aqueous-phase processing on aerosol chemistry and size distributions in Fresno, California, during wintertime, Environ. Chem., 9, 221-235, 10.1071/EN11168, 2012a.

Ge, X. L., Setyan, A., Sun, Y., and Zhang, Q.: Primary and secondary organic aerosols in Fresno, California during wintertime: Results from high resolution aerosol mass spectrometry, J. Geophys. Res. - Atmos., 117, D19301, 10.1029/2012jd018026, 2012b.

Ghan, S. J., and Schwartz, S. E.: Aerosol properties and processes: A path from field and laboratory measurements to global climate models, Bull. Am. Meteorol. Soc., 88, 1059-1083, 10.1175/bams-88-7-1059, 2007.

Han, T., Xu, W., Chen, C., Liu, X., Wang, Q., Li, J., Zhao, X., Du, W., Wang, Z., and Sun, Y.: Chemical apportionment of aerosol optical properties during the Asia-Pacific Economic Cooperation summit in Beijing, China, J. Geophys. Res. - Atmos., 120, 12,281-212,295, 10.1002/2015JD023918, 2015.

He, L. Y., Huang, X.-F., Xue, L., Hu, M., Lin, Y., Zheng, J., Zhang, R., and Zhang, Y.-H.: Submicron aerosol analysis and organic source apportionment in an urban atmosphere in Pearl River Delta of China using high-resolution aerosol mass spectrometry, J. Geophys. Res. - Atmos., 116, D12304, 10.1029/2010jd014566, 2011.

Heald, C. L., Kroll, J. H., Jimenez, J. L., Docherty, K. S., DeCarlo, P. F., Aiken, A. C., Chen, Q., Martin, S. T., Farmer, D. K., and Artaxo, P.: A simplified description of the evolution of organic aerosol composition in the atmosphere, Geophys. Res. Lett., 37, L08803, 10.1029/2010gl042737, 2010.

Hu, J., Ying, Q., Wang, Y., and Zhang, H.: Characterizing multi-pollutant air pollution in China: Comparison of three air quality indices, Environ. Int., 84, 17-25, 10.1016/j.envint.2015.06.014, 2015.

Hu, W. W., Hu, M., Yuan, B., Jimenez, J. L., Tang, Q., Peng, J. F., Hu, W., Shao, M., Wang, M., Zeng, L. M., Wu, Y. S., Gong, Z. H., Huang, X. F., and He, L. Y.: Insights on organic

745 aerosol aging and the influence of coal combustion at a regional receptor site of central
746 eastern China, Atmos. Chem. Phys., 13, 10095-10112, 10.5194/acp-13-10095-2013, 2013.

747 Hu, X., Zhang, Y., Ding, Z. H., Wang, T. J., Lian, H. Z., Sun, Y. Y., and Wu, J. C.:
748 Bioaccessibility and health risk of arsenic and heavy metals (Cd, Co, Cr, Cu, Ni, Pb, Zn and
749 Mn) in TSP and $PM_{2.5}$ in Nanjing, China, Atmos. Environ., 57, 146-152,
750 10.1016/j.atmosenv.2012.04.056, 2012.

751 Huang, X., Xue, L., Tian, X.-D., Shao, W.-W., Sun, T.-L., Gong, Z.-H., Ju, W.-W., Jiang, B.,
752 Hu, M., and He, L.-Y.: Highly time-resolved carbonaceous aerosol characterization in Yangtze
753 River Delta of China: composition, mixing state and secondary formation, Atmos. Environ.,
754 10.1016/j.atmosenv.2012.09.059, 2012a.

755 Huang, X. F., He, L. Y., Hu, M., Canagaratna, M. R., Sun, Y., Zhang, Q., Zhu, T., Xue, L.,
756 Zeng, L. W., Liu, X. G., Zhang, Y. H., Jayne, J. T., Ng, N. L., and Worsnop, D. R.: Highly
757 time-resolved chemical characterization of atmospheric submicron particles during 2008
758 Beijing Olympic Games using an Aerodyne High-Resolution Aerosol Mass Spectrometer,
759 Atmos. Chem. Phys., 10, 8933-8945, 10.5194/acp-10-8933-2010, 2010.

760 Huang, X. F., He, L. Y., Hu, M., Canagaratna, M. R., Kroll, J. H., Ng, N. L., Zhang, Y. H., Lin,
761 Y., Xue, L., Sun, T. L., Liu, X. G., Shao, M., Jayne, J. T., and Worsnop, D. R.:
762 Characterization of submicron aerosols at a rural site in Pearl River Delta of China using an
763 Aerodyne High-Resolution Aerosol Mass Spectrometer, Atmos. Chem. Phys., 11, 1865-1877,
764 10.5194/acp-11-1865-2011, 2011.

765 Huang, X. F., He, L. Y., Xue, L., Sun, T. L., Zeng, L. W., Gong, Z. H., Hu, M., and Zhu, T.:
766 Highly time-resolved chemical characterization of atmospheric fine particles during 2010
767 Shanghai World Expo, Atmos. Chem. Phys., 12, 4897-4907, 10.5194/acp-12-4897-2012,
768 2012b.

769 Jayne, J. T., Leard, D. C., Zhang, X., Davidovits, P., Smith, K. A., Kolb, C. E., and Worsnop,
770 D. R.: Development of an Aerosol Mass Spectrometer for Size and Composition Analysis of
771 Submicron Particles, Aerosol Sci. Tech., 33, 49 - 70, 10.1016/S0021-8502(98)00158-X, 2000.

772 Jiang, Q., Sun, Y. L., Wang, Z., and Yin, Y.: Aerosol composition and sources during the
773 Chinese Spring Festival: fireworks, secondary aerosol, and holiday effects, Atmos. Chem.
774 Phys., 15, 6023-6034, 10.5194/acp-15-6023-2015, 2015.

775 Jimenez, J. L., Jayne, J. T., Shi, Q., Kolb, C. E., Worsnop, D. R., Yourshaw, I., Seinfeld, J. H.,
776 Flagan, R. C., Zhang, X. F., Smith, K. A., Morris, J. W., and Davidovits, P.: Ambient aerosol
777 sampling using the Aerodyne Aerosol Mass Spectrometer, J. Geophys. Res. - Atmos., 108,
778 8425, 10.1029/2001jd001213, 2003.

779 Jimenez, J. L., Canagaratna, M. R., Donahue, N. M., Prevot, A. S. H., Zhang, Q., Kroll, J. H.,
780 DeCarlo, P. F., Allan, J. D., Coe, H., Ng, N. L., Aiken, A. C., Docherty, K. S., Ulbrich, I. M.,
781 Grieshop, A. P., Robinson, A. L., Duplissy, J., Smith, J. D., Wilson, K. R., Lanz, V. A.,

782 Hueglin, C., Sun, Y. L., Tian, J., Laaksonen, A., Raatikainen, T., Rautiainen, J., Vaattovaara, P.,
783 Ehn, M., Kulmala, M., Tomlinson, J. M., Collins, D. R., Cubison, M. J., Dunlea, E. J.,
784 Huffman, J. A., Onasch, T. B., Alfarra, M. R., Williams, P. I., Bower, K., Kondo, Y., Schneider,
785 J., Drewnick, F., Borrmann, S., Weimer, S., Demerjian, K., Salcedo, D., Cottrell, L., Griffin,
786 R., Takami, A., Miyoshi, T., Hatakeyama, S., Shimono, A., Sun, J. Y., Zhang, Y. M., Dzepina,
787 K., Kimmel, J. R., Sueper, D., Jayne, J. T., Herndon, S. C., Trimborn, A. M., Williams, L. R.,
788 Wood, E. C., Middlebrook, A. M., Kolb, C. E., Baltensperger, U., and Worsnop, D. R.:
789 Evolution of organic aerosols in the atmosphere, Science, 326, 1525-1529,
790 10.1126/science.1180353, 2009.

791 Kong, S. F., Li, L., Li, X. X., Yin, Y., Chen, K., Liu, D. T., Yuan, L., Zhang, Y. J., Shan, Y. P.,
792 and Ji, Y. Q.: The impacts of firework burning at the Chinese Spring Festival on air quality:
793 insights of tracers, source evolution and aging processes, Atmos. Chem. Phys., 15, 2167-2184,
794 10.5194/acp-15-2167-2015, 2015.

795 Kulmala, M., Lappalainen, H. K., Petäjä, T., Kurten, T., Kerminen, V. M., Viisanen, Y., Hari,
796 P., Sorvari, S., Bäck, J., Bondur, V., Kasimov, N., Kotlyakov, V., Matvienko, G., Baklanov, A.,
797 Guo, H. D., Ding, A., Hansson, H. C., and Zilitinkevich, S.: Introduction: The Pan-Eurasian
798 Experiment (PEEX) – multidisciplinary, multiscale and multicomponent research and
799 capacity-building initiative, Atmos. Chem. Phys., 15, 13085-13096,
800 10.5194/acp-15-13085-2015, 2015.

801 Lee, A. K. Y., Hayden, K. L., Herckes, P., Leaitch, W. R., Liggio, J., Macdonald, A. M., and
802 Abbatt, J. P. D.: Characterization of aerosol and cloud water at a mountain site during WACS
803 2010: secondary organic aerosol formation through oxidative cloud processing, Atmos. Chem.
804 Phys., 12, 7103-7116, 10.5194/acp-12-7103-2012, 2012.

805 Lee, B. P., Li, Y. J., Yu, J. Z., Louie, P. K. K., and Chan, C. K.: Physical and chemical
806 characterization of ambient aerosol by HR-ToF-AMS at a suburban site in Hong Kong during
807 springtime 2011, J. Geophys. Res. - Atmos., 118, 8625-8639, 10.1002/jgrd.50658, 2013.

808 Li, Y. J., Lee, B. P., Su, L., Fung, J. C. H., and Chan, C. K.: Seasonal characteristics of fine
809 particulate matter (PM) based on high-resolution time-of-flight aerosol mass spectrometric
810 (HR-ToF-AMS) measurements at the HKUST Supersite in Hong Kong, Atmos. Chem. Phys.,
811 15, 37-53, 10.5194/acp-15-37-2015, 2015.

812 Malm, W. C., and Day, D. E.: Estimates of aerosol species scattering characteristics as a
813 function of relative humidity, Atmos. Environ., 35, 2845-2860,
814 10.1016/S1352-2310(01)00077-2, 2001.

815 Matthew, B. M., Middlebrook, A. M., and Onasch, T. B.: Collection Efficiencies in an
816 Aerodyne Aerosol Mass Spectrometer as a Function of Particle Phase for Laboratory
817 Generated Aerosols, Aerosol Sci.Tech., 42, 884-898, 10.1080/02786820802356797, 2008.

818 Middlebrook, A. M., Bahreini, R., Jimenez, J. L., and Canagaratna, M. R.: Evaluation of
819 Composition-Dependent Collection Efficiencies for the Aerodyne Aerosol Mass Spectrometer

820   using Field Data, Aerosol Sci. Tech., 46, 258-271, 10.1080/02786826.2011.620041, 2012.

821   Mohr, C., DeCarlo, P. F., Heringa, M. F., Chirico, R., Slowik, J. G., Richter, R., Reche, C.,
822   Alastuey, A., Querol, X., Seco, R., Peñuelas, J., Jiménez, J. L., Crippa, M., Zimmermann, R.,
823   Baltensperger, U., and Prévôt, A. S. H.: Identification and quantification of organic aerosol
824   from cooking and other sources in Barcelona using aerosol mass spectrometer data, Atmos.
825   Chem. Phys., 12, 1649-1665, 10.5194/acp-12-1649-2012, 2012.

826   Mohr, C., DeCarlo, P. F., Heringa, M. F., Chirico, R., Richter, R., Crippa, M., Querol, X.,
827   Baltensperger, U., and Prévôt, A. S. H.: Spatial Variation of Aerosol Chemical Composition
828   and Organic Components Identified by Positive Matrix Factorization in the Barcelona Region,
829   Environ. Sci. Technol., 49, 10421-10430, 10.1021/acs.est.5b02149, 2015.

830   Ng, N. L., Canagaratna, M. R., Zhang, Q., Jimenez, J. L., Tian, J., Ulbrich, I. M., Kroll, J. H.,
831   Docherty, K. S., Chhabra, P. S., Bahreini, R., Murphy, S. M., Seinfeld, J. H., Hildebrandt, L.,
832   Donahue, N. M., DeCarlo, P. F., Lanz, V. A., Prevot, A. S. H., Dinar, E., Rudich, Y., and
833   Worsnop, D. R.: Organic aerosol components observed in Northern Hemispheric datasets
834   from Aerosol Mass Spectrometry, Atmos. Chem. Phys., 10, 4625-4641,
835   10.5194/acp-10-4625-2010, 2010.

836   Ng, N. L., Herndon, S. C., Trimborn, A., Canagaratna, M. R., Croteau, P. L., Onasch, T. B.,
837   Sueper, D., Worsnop, D. R., Zhang, Q., Sun, Y. L., and Jayne, J. T.: An Aerosol Chemical
838   Speciation Monitor (ACSM) for Routine Monitoring of the Composition and Mass
839   Concentrations of Ambient Aerosol, Aerosol Sci. Tech., 45, 770-784,
840   10.1080/02786826.2011.560211, 2011.

841   Onasch, T. B., Trimborn, A., Fortner, E. C., Jayne, J. T., Kok, G. L., Williams, L. R.,
842   Davidovits, P., and Worsnop, D. R.: Soot particle aerosol mass spectrometer: Development,
843   validation, and initial application, Aerosol Sci. Tech., 46, 804-817,
844   10.1080/02786826.2012.663948, 2012.

845   Onasch, T. B., Fortner, E. C., Trimborn, A. M., Lambe, A. T., Tiwari, A. J., Marr, L. C.,
846   Corbin, J. C., Mensah, A. A., Williams, L. R., Davidovits, P., and Worsnop, D. R.:
847   Investigations of SP-AMS Carbon Ion Distributions as a Function of Refractory Black
848   Carbon Particle Type, Aerosol Sci. Tech. , 49, 409-422, 10.1080/02786826.2015.1039959,
849   2015.

850   Paatero, P., and Tapper, U.: Positive matrix factorization: A non-negative factor model with
851   optimal utilization of error estimates of data values, Environmetrics, 5, 111-126,
852   10.1002/env.3170050203, 1994.

853   Pope, C. A., and Dockery, D. W.: Health Effects of Fine Particulate Air Pollution: Lines that
854   Connect, J. Air Waste Manage., 56, 709-742, 10.1080/10473289.2006.10464485, 2006.

855   Pöschl, U.: Atmospheric Aerosols: Composition, Transformation, Climate and Health Effects,
856   Angewandte Chemie International Edition, 44, 7520-7540, 10.1002/anie.200501122, 2005.

857 Qi, L., Zhang, Y., Ma, Y., Chen, M., Ge, X., Ma, Y., Zheng, J., Wang, Z., and Li, S.: Source
858 identification of trace elements in the atmosphere during the second Asian Youth Games in
859 Nanjing, China: Influence of control measures on air quality, Atmos. Pollut. Res., 7, 547-556,
860 http://dx.doi.org/10.1016/j.apr.2016.01.003, 2016.

861 Seinfeld, J. H., and Pandis, S. N.: Atmospheric Chemistry and Physics: From Air Pollution to
862 Climate Change, John Wiley & Sons, New York, 2006.

863 Setyan, A., Zhang, Q., Merkel, M., Knighton, W. B., Sun, Y., Song, C., Shilling, J. E., Onasch,
864 T. B., Herndon, S. C., Worsnop, D. R., Fast, J. D., Zaveri, R. A., Berg, L. K., Wiedensohler, A.,
865 Flowers, B. A., Dubey, M. K., and Subramanian, R.: Characterization of submicron particles
866 influenced by mixed biogenic and anthropogenic emissions using high-resolution aerosol
867 mass spectrometry: results from CARES, Atmos. Chem. Phys., 12, 8131-8156,
868 10.5194/acp-12-8131-2012, 2012.

869 Shen, G. F., Yuan, S. Y., Xie, Y. N., Xia, S. J., Li, L., Yao, Y. K., Qiao, Y. Z., Zhang, J., Zhao,
870 Q. Y., Ding, A. J., Li, B., and Wu, H. S.: Ambient levels and temporal variations of $PM_{2.5}$ and
871 PM_{10} at a residential site in the mega-city, Nanjing, in the western Yangtze River Delta, China,
872 J. Environ. Sci. Health., Part A, 49, 171-178, 10.1080/10934529.2013.838851, 2014.

873 Shen, X. J., Sun, J. Y., Zhang, X. Y., Zhang, Y. M., Zhang, L., Che, H. C., Ma, Q. L., Yu, X.
874 M., Yue, Y., and Zhang, Y. W.: Characterization of submicron aerosols and effect on visibility
875 during a severe haze-fog episode in Yangtze River Delta, China, Atmos. Environ., 120,
876 307-316, 10.1016/j.atmosenv.2015.09.011, 2015.

877 Sun, Y., Jiang, Q., Wang, Z., Fu, P., Li, J., Yang, T., and Yin, Y.: Investigation of the Sources
878 and Evolution Processes of Severe Haze Pollution in Beijing in January 2013, J. Geophys.
879 Res. - Atmos., 2014JD021641, 10.1002/2014JD021641, 2014.

880 Sun, Y. L., Zhang, Q., Schwab, J. J., Demerjian, K. L., Chen, W. N., Bae, M. S., Hung, H. M.,
881 Hogrefe, O., Frank, B., Rattigan, O. V., and Lin, Y. C.: Characterization of the sources and
882 processes of organic and inorganic aerosols in New York city with a high-resolution
883 time-of-flight aerosol mass apectrometer, Atmos. Chem. Phys., 11, 1581-1602,
884 10.5194/acp-11-1581-2011, 2011.

885 Sun, Y. L., Du, W., Wang, Q., Zhang, Q., Chen, C., Chen, Y., Chen, Z., Fu, P., Wang, Z., Gao,
886 Z., and Worsnop, D. R.: Real-Time Characterization of Aerosol Particle Composition above
887 the Urban Canopy in Beijing: Insights into the Interactions between the Atmospheric
888 Boundary Layer and Aerosol Chemistry, Environ. Sci. Technol., 49, 11340-11347,
889 10.1021/acs.est.5b02373, 2015a.

890 Sun, Y. L., Wang, Z. F., Du, W., Zhang, Q., Wang, Q. Q., Fu, P. Q., Pan, X. L., Li, J., Jayne, J.,
891 and Worsnop, D. R.: Long-term real-time measurements of aerosol particle composition in
892 Beijing, China: seasonal variations, meteorological effects, and source analysis, Atmos. Chem.
893 Phys., 15, 10149-10165, 10.5194/acp-15-10149-2015, 2015b.

894 Sun, Y. L., Wang, Z., Wild, O., Xu, W., Chen, C., Fu, P., Du, W., Zhou, L., Zhang, Q., Han, T.,
895 Wang, Q., Pan, X., Zheng, H., Li, J., Guo, X., Liu, J., and Worsnop, D. R.: "APEC Blue":
896 Secondary Aerosol Reductions from Emission Controls in Beijing, Sci. Rep., 6, 20668,
897 10.1038/srep20668, 2016.

898 Tang, L., Yu, H., Ding, A., Zhang, Y., Qin, W., Wang, Z., Chen, W., Hua, Y., and Yang, X.:
899 Regional contribution to PM1 pollution during winter haze in Yangtze River Delta, China, Sci.
900 Total Environ., 541, 161-166, 10.1016/j.scitotenv.2015.05.058, 2016.

901 Ulbrich, I. M., Canagaratna, M. R., Zhang, Q., Worsnop, D. R., and Jimenez, J. L.:
902 Interpretation of organic components from Positive Matrix Factorization of aerosol mass
903 spectrometric data, Atmos. Chem. Phys., 9, 2891-2918, 10.5194/acp-9-2891-2009, 2009.

904 Wang, G. H., Niu, S. L., Liu, C., and Wang, L. S.: Identification of dicarboxylic acids and
905 aldehyde of PM_{10} and $PM_{2.5}$ aerosols in Nanjing, China, Atmos. Environ., 36, 1941-1950,
906 10.1016/s1352-2310(02)00180-2, 2002.

907 Wang, G. H., Wang, H., Yu, Y. J., Gao, S. X., Feng, J. F., Gao, S. T., and Wang, L. S.:
908 Chemical characterization of water-soluble components of PM_{10} and $PM_{2.5}$ atmospheric
909 aerosols in five locations of Nanjing, China, Atmos. Environ., 37, 2893-2902,
910 10.1016/s1352-2310(03)00271-1, 2003.

911 Wang, G. H., Kawamura, K., Xie, M. J., Hu, S. Y., Cao, J. J., An, Z. S., Waston, J. G., and
912 Chow, J. C.: Organic molecular compositions and size distributions of Chinese summer and
913 autumn aerosols from Nanjing: Characteristic haze event caused by wheat straw burning,
914 Environ. Sci. Technol., 43, 6493-6499, 10.1021/es803086g, 2009.

915 Wang, G. H., Chen, C. L., Li, J. J., Zhou, B. H., Xie, M. J., Hu, S. Y., Kawamura, K., and
916 Chen, Y.: Molecular composition and size distribution of sugars, sugar-alcohols and
917 carboxylic acids in airborne particles during a severe urban haze event caused by wheat straw
918 burning, Atmos. Environ., 45, 2473-2479, 10.1016/j.atmosenv.2011.02.045, 2011.

919 Wang, J., Onasch, T. B., Ge, X., Collier, S., Zhang, Q., Sun, Y., Yu, H., Chen, M., Prévôt, A. S.
920 H., and Worsnop, D. R.: Observation of Fullerene Soot in Eastern China, Environ. Sci.
921 Technol. Lett., 3, 121-126, 10.1021/acs.estlett.6b00044, 2016a.

922 Wang, Q., Sun, Y., Jiang, Q., Du, W., Sun, C., Fu, P., and Wang, Z.: Chemical composition of
923 aerosol particles and light extinction apportionment before and during the heating season in
924 Beijing, China, J. Geophys. Res. - Atmos., 120, 2015JD023871, 10.1002/2015JD023871,
925 2015.

926 Wang, Q., Zhao, J., Du, W., Ana, G., Wang, Z., Sun, L., Wang, Y., Zhang, F., Li, Z., Ye, X.,
927 and Sun, Y.: Characterization of submicron aerosols at a suburban site in central China, Atmos
928 Environ, 131, 115-123, http://dx.doi.org/10.1016/j.atmosenv.2016.01.054, 2016b.

929 Wexler, A. S., and Johnston, M. V.: What have we learned from highly time-resolved

930 measurements during EPA's Supersites program,and related studies?, J. Air Waste Manage.,
931 58, 303-319, 10.3155/1047-3289.58.2.303, 2008.

932 Xu, J., Zhang, Q., Chen, M., Ge, X., Ren, J., and Qin, D.: Chemical composition, sources, and
933 processes of urban aerosols during summertime in northwest China: insights from
934 high-resolution aerosol mass spectrometry, Atmos. Chem. Phys., 14, 12593-12611,
935 10.5194/acp-14-12593-2014, 2014.

936 Xu, W. Q., Sun, Y. L., Chen, C., Du, W., Han, T. T., Wang, Q. Q., Fu, P. Q., Wang, Z. F., Zhao,
937 X. J., Zhou, L. B., Ji, D. S., Wang, P. C., and Worsnop, D. R.: Aerosol composition, oxidation
938 properties, and sources in Beijing: results from the 2014 Asia-Pacific Economic Cooperation
939 summit study, Atmos. Chem. Phys., 15, 13681-13698, 10.5194/acp-15-13681-2015, 2015.

940 Yan, J., Chen, L., Lin, Q., Li, Z., Chen, H., and Zhao, S.: Chemical characteristics of
941 submicron aerosol particles during a long-lasting haze episode in Xiamen, China, Atmos.
942 Environ., 113, 118-126, 10.1016/j.atmosenv.2015.05.003, 2015.

943 Yang, H., Yu, J. Z., Ho, S. S. H., Xu, J. H., Wu, W. S., Wan, C. H., Wang, X. D., Wang, X. R.,
944 and Wang, L. S.: The chemical composition of inorganic and carbonaceous materials in $PM_{2.5}$
945 in Nanjing, China, Atmos. Environ., 39, 3735-3749, 10.1016/j.atmosenv.2005.03.010, 2005.

946 Yang, L.-X., Wang, D.-c., Cheng, S.-h., Wang, Z., Zhou, Y., Zhou, X.-h., and Wang, W.-x.:
947 Influence of meteorological conditions and particulate matter on visual range impairment in
948 Jinan, China, Sci. Total Environ., 383, 164-173, 10.1016/j.scitotenv.2007.04.042, 2007.

949 Yeung, M. C., Lee, B. P., Li, Y. J., and Chan, C. K.: Simultaneous HTDMA and
950 HR-ToF-AMS measurements at the HKUST Supersite in Hong Kong in 2011, J. Geophys.
951 Res. - Atmos., 2013JD021146, 10.1002/2013JD021146, 2014.

952 Young, D. E., Kim, H., Parworth, C., Zhou, S., Zhang, X., Cappa, C. D., Seco, R., Kim, S.,
953 and Zhang, Q.: Influences of emission sources and meteorology on aerosol chemistry in a
954 polluted urban environment: results from DISCOVER-AQ California, Atmos. Chem. Phys.,
955 16, 5427-5451, 10.5194/acp-16-5427-2016, 2016.

956 Yu, L., Smith, J., Laskin, A., Anastasio, C., Laskin, J., and Zhang, Q.: Chemical
957 characterization of SOA formed from aqueous-phase reactions of phenols with the triplet
958 excited state of carbonyl and hydroxyl radical, Atmos. Chem. Phys., 14, 13801-13816,
959 10.5194/acp-14-13801-2014, 2014.

960 Zhang, J. K., Sun, Y., Liu, Z. R., Ji, D. S., Hu, B., Liu, Q., and Wang, Y. S.: Characterization
961 of submicron aerosols during a month of serious pollution in Beijing, 2013, Atmos. Chem.
962 Phys., 14, 2887-2903, 10.5194/acp-14-2887-2014, 2014.

963 Zhang, J. K., Wang, L. L., Wang, Y. H., and Wang, Y. S.: Submicron aerosols during the
964 Beijing Asia–Pacific Economic Cooperation conference in 2014, Atmos. Environ., 124, Part
965 B, 224-231, 10.1016/j.scitotenv.2007.04.042, 2016a.

966 Zhang, Q., Alfarra, M. R., Worsnop, D. R., Allan, J. D., Coe, H., Canagaratna, M. R., and
967 Jimenez, J. L.: Deconvolution and quantification of hydrocarbon-like and oxygenated organic
968 aerosols based on aerosol mass spectrometry, Environ. Sci. Technol., 39, 4938-4952,
969 10.1021/Es048568l, 2005.

970 Zhang, Q., Jimenez, J. L., Canagaratna, M. R., Allan, J. D., Coe, H., Ulbrich, I., Alfarra, M. R.,
971 Takami, A., Middlebrook, A. M., Sun, Y. L., Dzepina, K., Dunlea, E., Docherty, K., DeCarlo,
972 P. F., Salcedo, D., Onasch, T., Jayne, J. T., Miyoshi, T., Shimono, A., Hatakeyama, S.,
973 Takegawa, N., Kondo, Y., Schneider, J., Drewnick, F., Borrmann, S., Weimer, S., Demerjian,
974 K., Williams, P., Bower, K., Bahreini, R., Cottrell, L., Griffin, R. J., Rautiainen, J., Sun, J. Y.,
975 Zhang, Y. M., and Worsnop, D. R.: Ubiquity and dominance of oxygenated species in organic
976 aerosols in anthropogenically-influenced Northern Hemisphere midlatitudes, Geophys. Res.
977 Lett., 34, L13801, 10.1029/2007gl029979, 2007a.

978 Zhang, Q., Jimenez, J. L., Worsnop, D. R., and Canagaratna, M.: A case study of urban
979 particle acidity and its influence on secondary organic aerosol, Environ. Sci. Technol., 41,
980 3213-3219, 10.1021/Es061812j, 2007b.

981 Zhang, Q., Jimenez, J., Canagaratna, M., Ulbrich, I., Ng, N., Worsnop, D., and Sun, Y.:
982 Understanding atmospheric organic aerosols via factor analysis of aerosol mass spectrometry:
983 a review, Anal. Bioanal. Chem., 401, 3045-3067, 10.1007/s00216-011-5355-y, 2011.

984 Zhang, Y. J., Tang, L. L., Wang, Z., Yu, H. X., Sun, Y. L., Liu, D., Qin, W., Canonaco, F.,
985 Prévôt, A. S. H., Zhang, H. L., and Zhou, H. C.: Insights into characteristics, sources, and
986 evolution of submicron aerosols during harvest seasons in the Yangtze River delta region,
987 China, Atmos. Chem. Phys., 15, 1331-1349, 10.5194/acp-15-1331-2015, 2015.

988 Zhang, Y. J., Tang, L., Yu, H., Wang, Z., Sun, Y., Qin, W., Chen, W., Chen, C., Ding, A., Wu,
989 J., Ge, S., Chen, C., and Zhou, H.-c.: Chemical composition, sources and evolution processes
990 of aerosol at an urban site in Yangtze River Delta, China during wintertime, Atmos. Environ.,
991 123, 339-349, 10.1016/j.atmosenv.2015.08.017, 2016b.
992
993
994
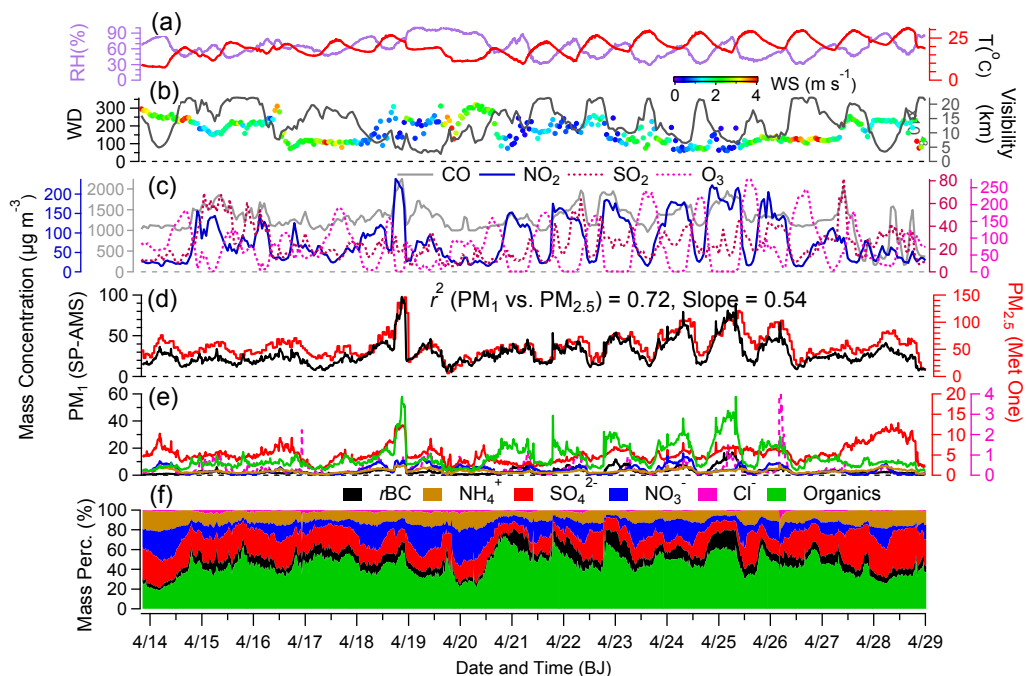
995

996 Figure 1. Time series of (a) relative humidity (RH) and temperature (T), (b) wind
997 direction (WD) colored by wind speed (WS, m s^{-1}) and visibility (km), (c) mass
998 concentrations of CO, NO$_2$, SO$_2$ and O$_3$ (hourly data), (d) mass concentrations of PM$_1$
999 measured by the SP-AMS, and PM$_{2.5}$ measured by the co-located Met One PM$_{2.5}$
1000 analyzer, (e) mass concentrations of rBC, ammonium, sulfate, nitrate, chloride and
1001 organics, and (f) mass contributions (%) of the six PM$_1$ components (BJ, Beijing).
1002

1003
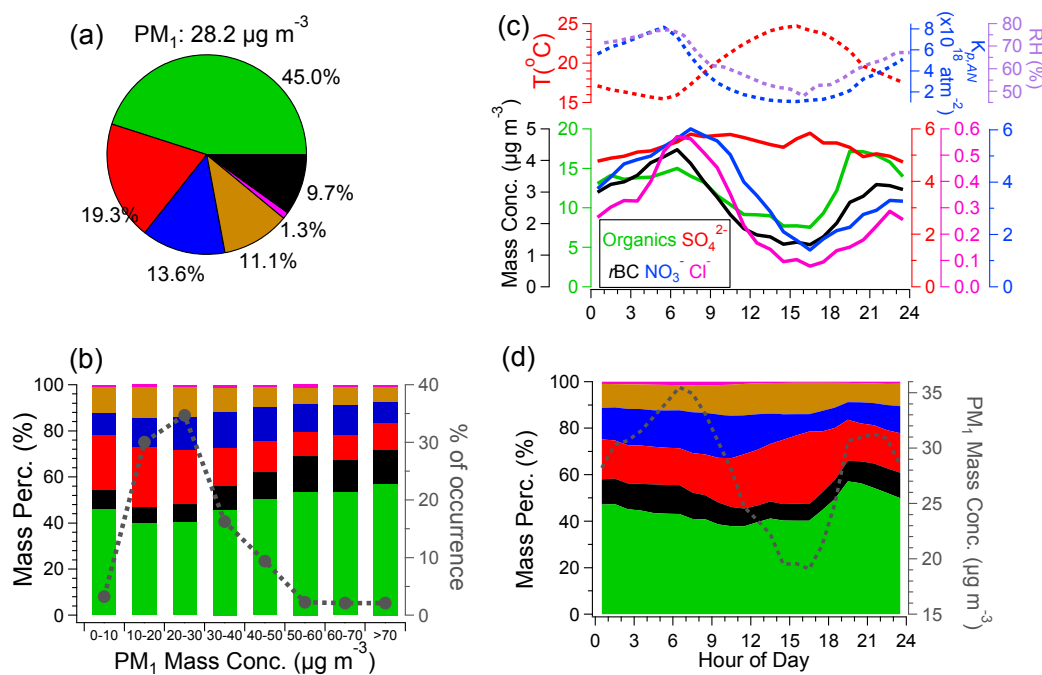
1004

1005

1006 Figure 2. (a) Campaign-averaged mass contributions of organics, sulfate, nitrate,
1007 ammonium, chloride and rBC to the total PM_1, (b) mass percentages of the six PM_1
1008 species (left y-axis) and, fractions of the number of data points to the total number of
1009 data points for PM_1 at different concentration bins (right y-axis), (c) diurnal patterns
1010 of mass concentrations of the major PM_1 species (bottom panel), temperature (top
1011 panel, left y-axis), relative humidity (RH) (top panel, right y-axis), and the equilibrium
1012 constant $(K_{p,AN})$ of NH_4NO_3 (top panel, right y-axis)

1013 ($K_{p,AN} = K_{p,AN}(298)exp\left\{a\left(\frac{298}{T}-1\right)+b\left[1+ln\left(\frac{298}{T}\right)-\frac{298}{T}\right]\right\}$, for reaction

1014 $NH_4NO_3(p) \leftrightarrow NH_3(g) + HNO_3(g)$. $K_{p,AN}(298)$ is the equilibrium constant at 298 K
1015 (3.36×10^{16} atm^{-2}), a = 75.11, and b = -13.5 (Seinfeld and Pandis, 2006)), (d) diurnal
1016 variations of mass fractional contributions of the six PM_1 species (left y-axis), and the
1017 PM_1 mass concentrations (right y-axis).

1018

1019
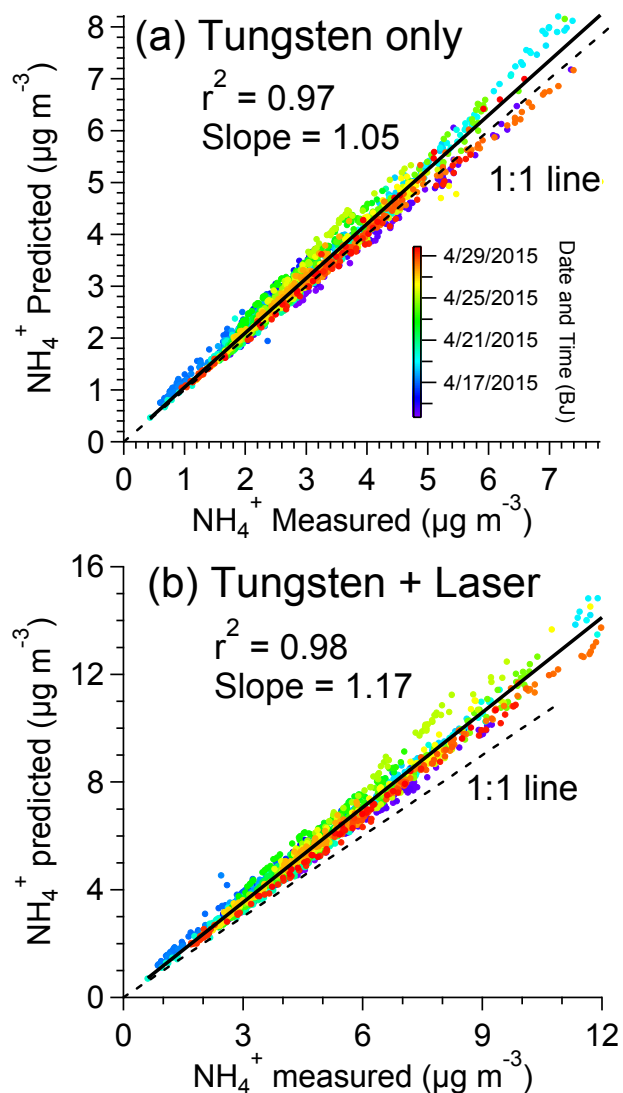
1020

1021 Figure 3. Scatter plots of the predicted NH_4^+ *vs.* measured NH_4^+ concentrations
1022 (colored by time), in the case of (a) tungsten vaporizer only, and (b) dual-vaporizers
1023 (tungsten + laser). The predicted values were calculated according to the formula:
1024 NH_4^+ predicted $= 18 \times (2 \times SO_4^{2-}/96 + NO_3^-/62 + Cl^-/35.5)$ (Zhang et al., 2007b).

1025
1026
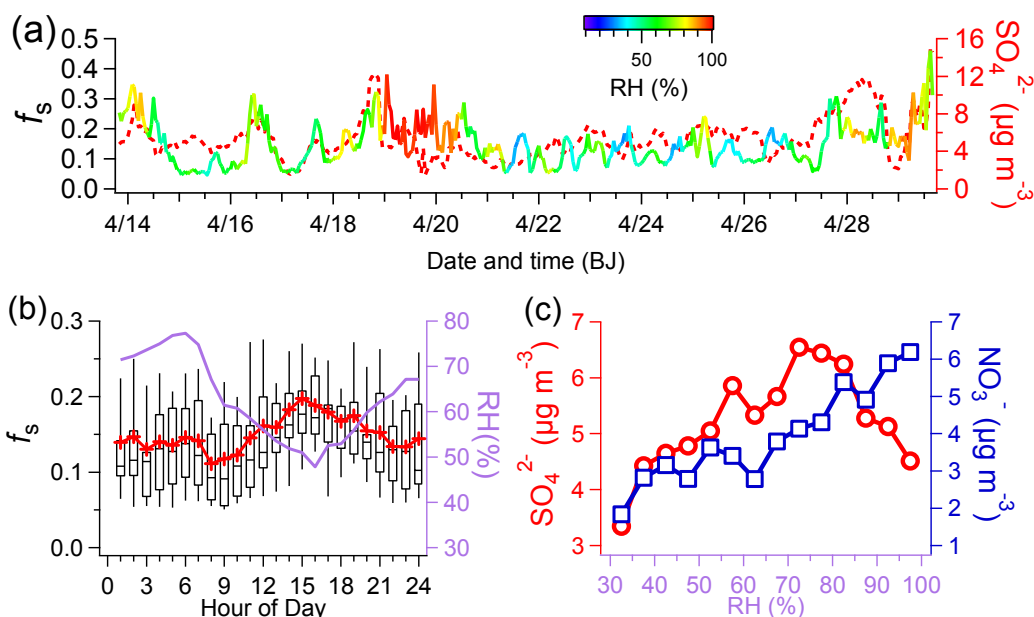
1029 Figure 4. Time series of (a) sulfur oxidation ratio, $f_S = nSO_4^{2-}/(nSO_4^{2-} + nSO_2)$, and
1030 sulfate, (b) diurnal variations of f_S and RH (the lines and cross symbols indicate the
1031 mean values, the lines in the boxes indicate the median values, the upper and lower
1032 boundaries of the boxes indicate the 75th and 25th percentiles, and the whiskers above
1033 and below the boxes indicate the 90th and 10th percentiles), (c) Sulfate and nitrate
1034 concentrations *vs.* RH, the circles or squares represent the average concentrations
1035 within different RH bins (5% increment) for sulfate and nitrate, respectively.

1036
1037
1038
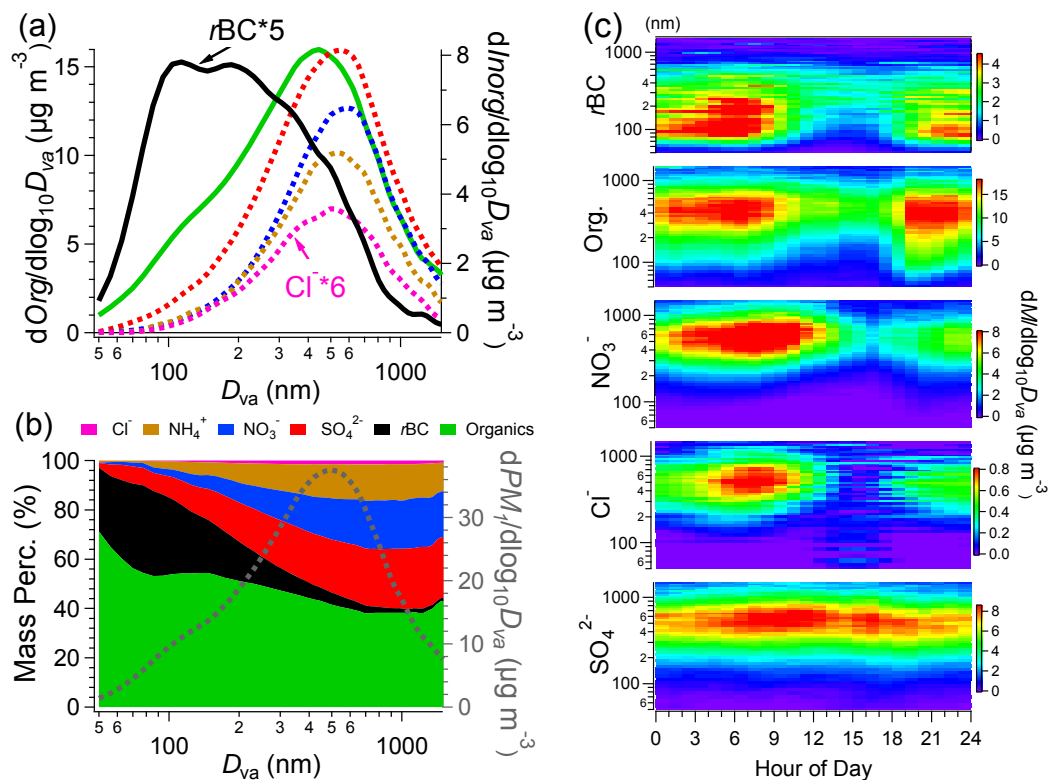
Figure 5. (a) Mass-based average size distributions of organics, rBC (left y-axis), sulfate, nitrate, chloride and ammonium (right y-axis) (D_{va}, vacuum aerodynamic diameter), (b) fractional contributions of the six PM_1 species as a function of particle size (left y-axis), and size distribution of total PM_1 (right y-axis), (c) diurnal profiles of the size distributions of rBC, organics, nitrate, chloride and sulfate.
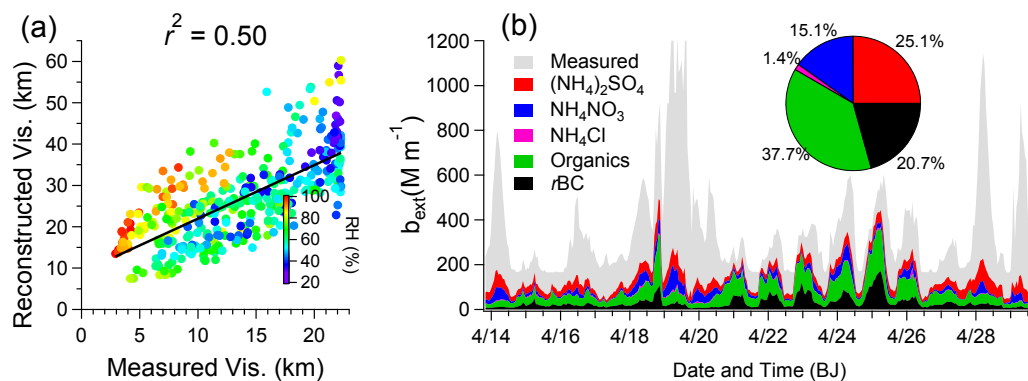
Figure 6. (a) Scatter plot of reconstructed *vs.* measured visibility (colored by RH), (b) light extinction coefficients derived from measured visibility (grey), and reconstructed from SP-AMS measured ammonium sulfate, ammonium nitrate, ammonium chloride, organics and *r*BC using the IMPROVE method. The inset pie shows the relative contributions of the five species to the light extinction of PM_1.
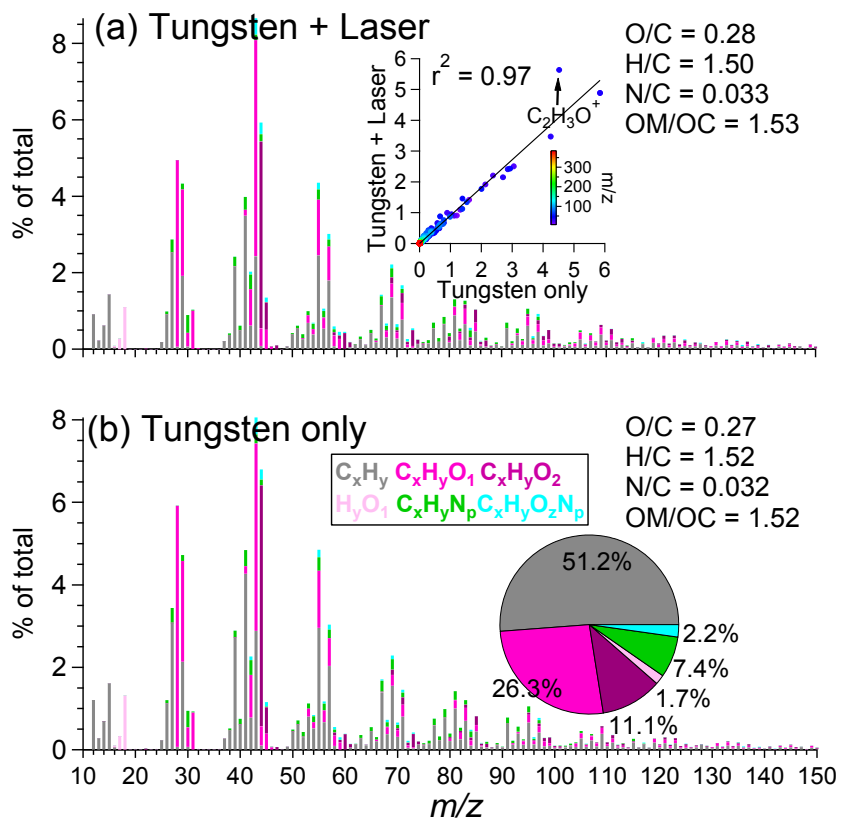
1055

Figure 7. Campaign-averaged high resolution mass spectra of OA colored by six ion
categories, in the case of (a) dual-vaporizers (tungsten + laser) (the inset scatter plot
compares the spectral similarity between (a) and (b)), and (b) tungsten vaporizer only
(the inset pie shows the relative contributions of six ion categories to the total OA).

1060
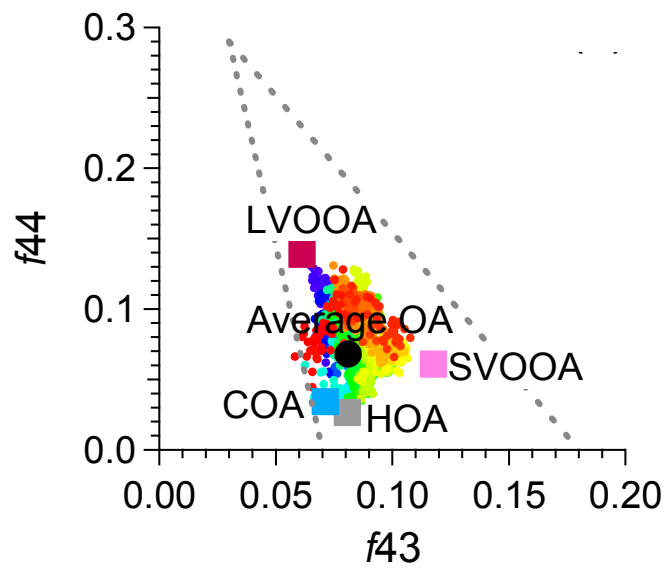
Figure 8. Triangle plot of $f44$ *vs.* $f43$ for all OA (colored by time), and the four OA factors identified by the PMF analyses.
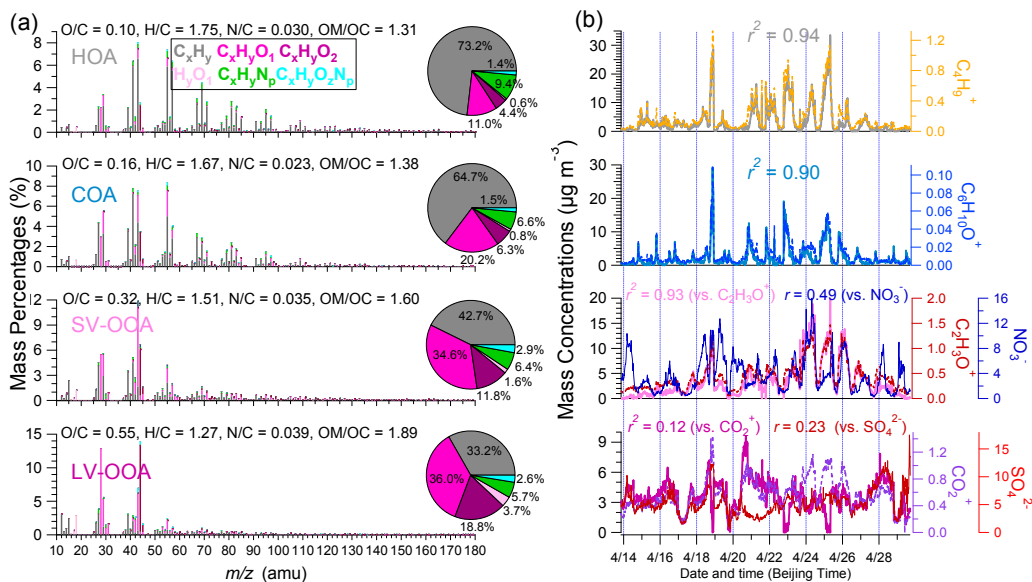
Figure 9. (a) High resolution mass spectra of hydrocarbon-like OA (HOA), cooking-related OA (COA), semi-volatile oxygenated OA (SV-OOA), and low volatility oxygenated OA (LV-OOA) colored by six ion categories (the four inset pies show the relative contributions of the six ion categories to the four OA factors, respectively), (b) time series of the four OA factors, corresponding tracer ions, nitrate and sulfate.
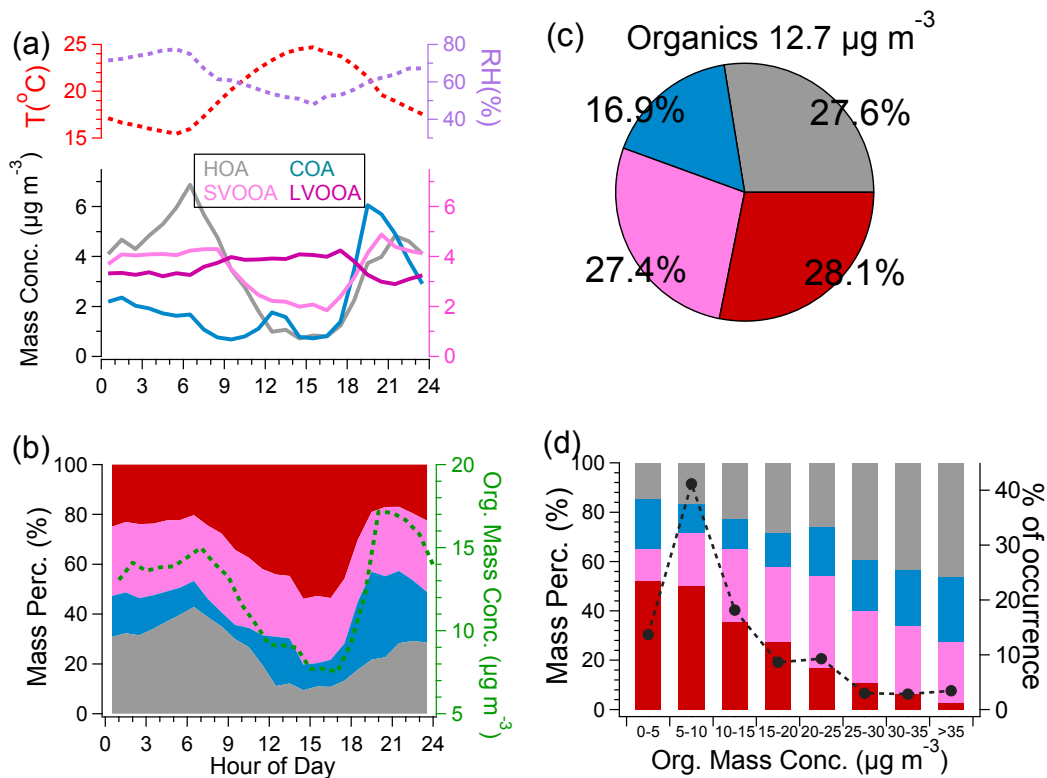
Figure 10. (a) Diurnal cycles of mass concentrations of the four OA factors (bottom panel), temperature (top panel, left *y*-axis) and RH (top panel, right *y*-axis), (b) diurnal variations of mass contributions of the four OA factors (left *y*-axis), and the total OA mass concentrations (right *y*-axis), (c) campaign-averaged mass contributions of the four OA factors to the total OA mass, and (d) mass contributions of the four OA factors (left *y*-axis), and the fractions of the number of data points to the total number of data points for the OA at different concentration ranges (right *y*-axis).
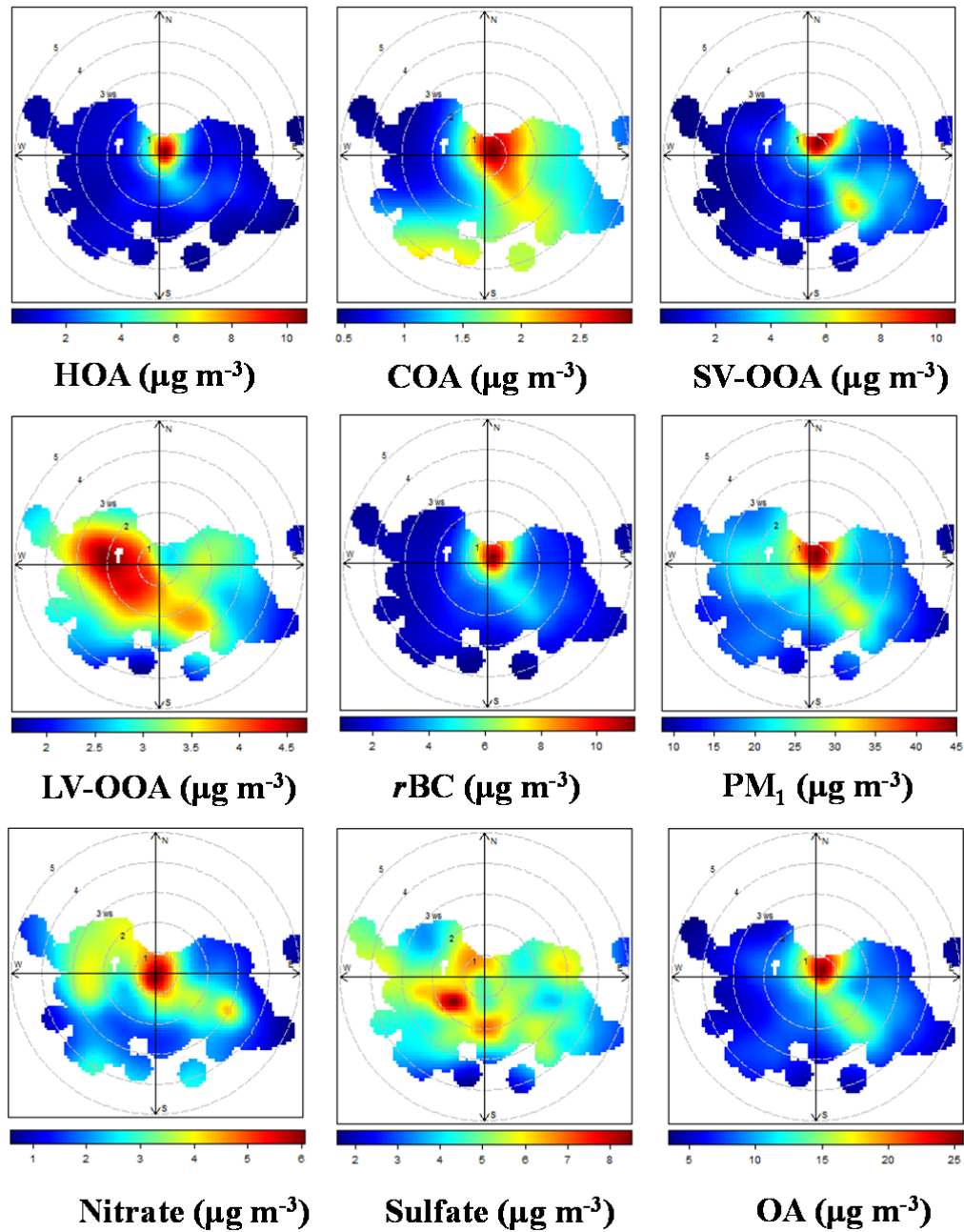
Figure 11. Bivariate polar plots of HOA, COA, SV-OOA, LV-OOA, rBC, PM$_1$, nitrate, sulfate and the total OA (the color scale shows the concentration of each species, and the radical scale shows the wind speed that increases outward from the center).

1096

1097
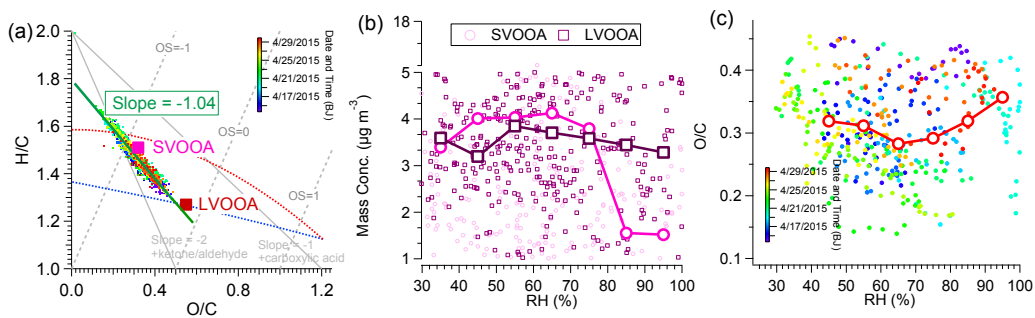
1098

1099 Figure 12. (a) Van Krevelen diagram of H/C *vs.* O/C ratios for all OA data colored by
1100 time, the blue and red dashed lines correspond to the right and left grey dashed lines
1101 in the *f*44 vs. f43 triangle plot of Fig. 8, the grey lines represents the addition of a
1102 particular functional group to an aliphatic carbon (Heald et al., 2010), (b) scatter plot
1103 of SVOOA and LVOOA mass concentrations *vs.* RH, the circles or squares represent
1104 the average mass concentrations within different RH bins (10% increment) for
1105 SVOOA and LVOOA, respectively, (c) scatter plot of O/C *vs.* RH (colored by time),
1106 the circles represent the average O/C values within different RH bins (10%
1107 increment).

1108

1109 Table 1. Correlation coefficients (Pearson's r^2) between the mass spectral profiles of
1110 the OA factors identified in this work with the corresponding factors identified in
1111 Beijing (2013 Winter) (Sun et al., 2015a), Lanzhou (2014 Summer) ((Xu et al., 2014)),
1112 and Fresno (2010 Winter) (Ge et al., 2012b).

1113

Nanjing (2015 Spring)	High resolution MS (r^2)		
	Beijing (2013 Winter)	Lanzhou (2012 Summer)	Fresno (2010 Winter)*
HOA	0.92	0.90	0.98
COA	0.93	0.94	0.93
SV-OOA	0.68	0.75	0.90
LV-OOA	0.91	0.98	0.87
	Unit mass resolution MS (r^2)		
HOA	0.92	0.91	0.99
COA	0.96	0.96	0.95
SV-OOA	0.70	0.74	0.91
LV-OOA	0.90	0.98	0.89

1114 *Note the Fresno (2010 Winter) study only identified one OOA factor, we thus
1115 compared both SV-OOA and LV-OOA in this study with it.

1116 Table 2. Correlation coefficients (Pearson's r) between the time series of the four OA
1117 factors with the gas-phase species (hourly data) and other PM_1 components (15-min
1118 data), and the correlation coefficients between the diurnal data.
1119

Pearson's r	Temp.(T)	CO	NO_2	SO_2	O_3	SO_4^{2-}	NO_3^-	Cl^-	rBC
			Hourly data				15-min data		
HOA	-0.14	0.71	0.77	0.13	-0.54	0.15	0.26	0.45	0.92
COA	0.11	0.50	0.58	-0.06	-0.22	0.19	0.07	0.08	0.61
SVOOA	0.19	0.41	0.70	0.14	-0.21	0.11	0.49	0.25	0.70
LVOOA	0.069	-0.2	-0.18	0.06	0.14	0.23	0.11	0.01	-0.22
				Diurnal data					
HOA	-0.94	0.86	0.86	0.66	-0.96	-0.35	0.72	0.82	0.99
COA	-0.15	0.28	0.59	-0.24	-0.24	-0.57	-0.33	-0.25	0.19
SVOOA	-0.85	0.86	0.94	0.58	-0.90	-0.51	0.53	0.61	0.89
LVOOA	0.76	-0.58	-0.83	-0.27	0.77	0.72	-0.26	-0.33	-0.75

1120

1121